

# Tsunami Generation by Submarine Mass Failure. I: Modeling, Experimental Validation, and Sensitivity Analyses

Stéphan T. Grilli, M.ASCE,<sup>1</sup> and Philip Watts<sup>2</sup>

**Abstract:** Numerical simulations are performed with a two-dimensional (2D) fully nonlinear potential flow (FNPF) model for tsunami generation by two idealized types of submarine mass failure (SMF): underwater slides and slumps. These simulations feature rigid or deforming SMFs with a Gaussian cross section, translating down a plane slope. In each case, the SMF center of mass motion is expressed as a function of geometric, hydrodynamic, and material parameters, following a simple wavemaker formalism, and prescribed as a boundary condition in the FNPF model. Tsunami amplitudes and runup are obtained from computed free surface elevations. Model results are experimentally validated for a rigid 2D slide. Sensitivity studies are performed to estimate the effects of SMF-shape, type, and initial submergence depth—on the generated tsunamis. A strong SMF deformation during motion is shown to significantly enhance tsunami generation, particularly in the far-field. Typical slumps are shown to generate smaller tsunamis than corresponding slides. Both tsunami amplitude and runup are shown to depend strongly on initial SMF submergence depth. For the selected SMF idealized geometry, this dependence is simply expressed by power laws. Other sensitivity analyses are presented in a companion paper, and results from numerical simulations are converted into empirical curve fits predicting characteristic tsunami amplitudes as functions of nondimensional governing parameters. It should be stressed that these empirical formulas are only valid in the vicinity of the tsunami sources and, because of the complexity of the problem, many simplifications were necessary. It is further shown in the companion paper how 2D results can be modified to account for three-dimensional tsunami generation and used for quickly estimating tsunami hazard or for performing simple case studies.

**DOI:** 10.1061/(ASCE)0733-950X(2005)131:6(283)

**CE Database subject headings:** Tsunamis; Landslides; Experimentation; Boundary element method; Simulation; Sensitivity analysis.

## Introduction

Submarine mass failures (SMFs) refers to all submerged rock slides, reef failures, and many forms of sediment failure, creeping or inertial. SMF classification can be made on the basis of landslide morphology, landslide material, or landslide dynamics (Hampton et al. 1996; Turner and Schuster 1996; Keating and McGuire 2000). We will restrict this study to tsunami generation by two idealized types of SMF; underwater slides and slumps, which represent convenient end members for the general range of possible SMF motion. It is well understood that actual SMFs are more complex, but the analysis of tsunamis caused by slides and slumps may provide approximate upper and lower bounds for tsunami amplitudes to be expected in many situations, when the exact nature of the SMF is usually unknown. Slides can be defined as thin, translational failures traveling over long distances, and slumps can be defined as thick, rotational failures occurring with minimal displacement (Prior and Coleman 1979; Edgers and

Karlsrud 1982). According to Schwab et al. (1993), slumps represent approximately 50% of all SMFs.

Tsunami generation by SMF became an object of great concern in the research community following the 1998 Papua New Guinea event that caused great loss in human life (e.g., Synolakis et al. 2002; Tappin et al. 2001, 2002). Tsunamis generated by coseismic displacement are usually relatively small for moderate earthquakes, because tsunami amplitude correlates with earthquake moment magnitude. Tsunamis caused by SMFs, however, are only limited in amplitude by the SMF vertical displacement (Striem and Miloh 1976; Murty 1979; Watts 1998). Because SMFs usually occur on continental slopes, such displacements may reach several thousand meters and thereby produce huge tsunamis, regardless of earthquake magnitude. Moreover, these tsunamis offer little time for warning due to the proximity to shore of continental slopes. For all these reasons, tsunamis generated by SMFs may represent one of the major coastal hazards for moderate earthquakes.

Many tsunami generation, propagation, and runup models have been developed, including some specifically devoted to SMF tsunamis (as discussed hereafter). In Part I of this work, after validation with experiments, we use such a model—the two-dimensional (2D) tsunami generation model of Grilli and Watts (1999) (GW)—to perform sensitivity analyses and estimate effects of SMF shape, type, deformation, and initial submergence depth on the generated tsunami amplitude and runup. In Part II, the companion paper, we discuss some of the simplifying hypotheses introduced in Part I and show how to estimate three-dimensional (3D) effects on tsunami features. For rapid tsunami hazard assessment in a given situation, particularly during crises,

<sup>1</sup>Professor and Chair, Dept. of Ocean Engineering, Univ. of Rhode Island, Narragansett, RI 02882.

<sup>2</sup>President, Applied Fluids Engineering, Inc., Long Beach, CA 90803.

Note. Discussion open until April 1, 2006. Separate discussions must be submitted for individual papers. To extend the closing date by one month, a written request must be filed with the ASCE Managing Editor. The manuscript for this paper was submitted for review and possible publication on October 23, 2001; approved on March 29, 2005. This paper is part of the *Journal of Waterway, Port, Coastal, and Ocean Engineering*, Vol. 131, No. 6, November 1, 2005. ©ASCE, ISSN 0733-950X/2005/6-283-297/\$25.00.

it may be important to quickly predict reasonable SMF tsunami amplitudes, as a function of simple geological and geometrical parameters, without having to run extensive computations. Hence, in Part II, we derive simple predictive equations for 2D tsunami amplitude as a function of relevant nondimensional parameters, based on results of many computations with GW's model, for many idealized scenarios of slides and slumps. We show how such equations, combined with tsunami wavelength, can provide 2D free surface profile information in the vicinity of the source, in a large variety of situations. We further propose a method to infer 3D free surface elevations shortly after tsunami generation from the 2D predictive equations. Such 3D elevations can be used in case studies as input for standard long wave models of tsunami propagation (Watts et al. 2003). Finally, we give examples of the application of the predictive equations to a few historically significant case studies.

Laboratory and analytical studies of water waves generated by SMF have been conducted by Wiegel (1955), Iwasaki (1982), Heinrich (1992), Watts (1997, 1998, 2000), and Enet et al. (2003). 2D numerical simulations of water waves generated by SMF have been conducted by Iwasaki (1987, 1997) and Harbitz (1992) using linear shallow water wave (LSW) equations; by Verriere and Lenoir (1992) using linearized potential flow equations; by Heinrich (1992) and Assier-Rzadkiewicz et al. (1997) using a volume of fluid (VOF) solution of the Navier-Stokes (NS) equations; and by Jiang and LeBlond (1992, 1993, 1994), Imamura and Gica (1996), and Fine et al. (1998) using nonlinear shallow water wave (NSW) equations with a two-phase flow model. Other NSW landslide tsunami simulations can be found in Thomson et al. (2001) and Titov and Gonzales (2001). Some authors have studied SMF tsunamis using a Green's function representation of LSW, generated over constant depth by an SMF moving with uniform velocity (Tinti and Bortolucci 2000; Tinti et al. 2001; Todorovska et al. 2002; Ward 2001). Lynett and Liu (2003) derived fully nonlinear and dispersive long wave (Boussinesq) equations (BM) for submarine slides and implemented these in a model similar to that of Wei et al. (1995). They showed that both the runup and tsunami amplitude predicted for shallow 2D slides of Gaussian shape (i.e., for long waves as compared to depth) were in good agreement with exact results of a fully nonlinear potential flow (FNPF) model similar to that of GW. Larger discrepancies occurred for deeper slide submergence. For completion, smoothed particle hydrodynamics methods (SPH) were recently applied to the modeling of 2D (Fontaine 2000) and 3D (Gomez-Geisteira and Dalrymple 2004) wave interaction with structures and could offer a promising way of modeling complex SMF tsunami generation, particularly subaerial.

In GW, a 2D-FNPF model was applied to water wave generation by underwater landslides, following the wavemaker formalism of Watts (1998) to specify underwater landslide geometry and kinematics. Model governing equations were solved by a higher-order boundary element method (BEM). Time integration was based on second-order explicit Taylor series expansions of the free surface position and the velocity potential. The same model reproduced laboratory experiments for solitary wave shoaling and breaking on a slope to within a few percent (Grilli et al. 1994, 1997, 1998) and various other long-wave runup benchmark problems (Grilli 1997). GW performed a sensitivity analysis for only one underwater landslide scenario.

Making the usual nondimensional arguments for gravity waves, Watts (1998, 2000) noted that dispersive effects in SMF tsunamis can be expressed by a relative depth parameter,  $\mu = d/\lambda_o$ , where  $d$ =initial SMF submergence and  $\lambda_o$ =tsunami

wavelength. Similarly, nonlinear effects can be expressed by a steepness parameter  $a/\lambda_o$ , where  $a$ =tsunami amplitude. Estimating typical values of these parameters, it can further be shown that both nonlinear and dispersive effects are important for SMF tsunamis. This was one of the motivations for Lynett and Liu (2003) to derive and use a fully nonlinear BM rather than an NSW model to simulate SMF tsunami generation, and for Watts et al. (2003) to use the fully nonlinear BM of Wei et al. (1995) to model SMF tsunami propagation. However, as noted by the former authors, such depth-integrated equations are inaccurate for modeling tsunami generation when the SMF occurs in deeper water (about  $\mu > 1/7$ , in which we assumed the slide side length introduced in Lynett and Liu is about  $\lambda_o/2$ ). BM equations also cannot model waves close to breaking and, hence, are inaccurate for simulating very shallow and thick SMFs as well. GW's 2D-FNPF model, which is used here, features both fully nonlinear and dispersive effects, without any restriction on tsunami amplitude (except that wave overturning, although modeled, will stop computations), wavelength, or submergence depth. The FNPF assumption of inviscid, irrotational, flows is justified for modeling nonbreaking wave propagation, and a VOF solution of NS equations seems unnecessary, given the low viscosity of water (this will be confirmed by comparing results with experiments). These considerations justify the proposed modeling approach.

## Numerical Modeling

### SMF Geometry

We model tsunamis caused by SMFs moving parallel to a plane slope of angle  $\theta$  from horizontal (Fig. 1). We assume homogenous SMFs in the width direction and, hence, solve 2D problems in the vertical plane for slices of width  $w$ . We further assume nonseparated high Reynolds number flows around the moving SMFs, for which the fluid can be considered as inviscid. According to Kelvin's theorem applied from an initial state of rest, the flow is irrotational and can be represented by the velocity potential  $\phi$ , with velocity  $\mathbf{u} = \nabla\phi$ . Mass conservation yields a Laplace's equation for  $\phi$ , which is solved by a higher-order boundary element method (BEM) in GW's 2D-FNPF model. Given that an accurate SMF tsunami source geometry is rarely available, we represent SMFs by cross sections of idealized shape. GW used semielliptical shapes with maximum thickness  $T$  along the minor semiaxis, total length  $B$  along the major axis, and an initial vertical submergence  $d$  at the middle location. Here, we simulate more realistic SMF cross sections, represented by Gaussian shapes defined (Fig. 2) as

$$\zeta = \frac{T}{1 - \varepsilon} \{ \text{sech}^2(\kappa\xi) - \varepsilon \} \quad (1)$$

in which  $\varepsilon \in ]0, 1[$  is a spreading parameter. For comparison with earlier work, we assume that these SMFs have the same thickness  $T$  and volume  $V_\ell$  as semiellipses ( $B/2, T$ ), which yields

$$b = \frac{2C}{\kappa} \text{ and } \kappa = \frac{2C'}{B} \text{ with } C' = \frac{4(\tanh C - \varepsilon C)}{\pi(1 - \varepsilon)} \quad (2)$$

$$C = \text{acosh} \frac{1}{\sqrt{\varepsilon}}; \quad V_\ell = \frac{\pi}{4} wBT$$

where  $b(\varepsilon)$ =SMF length.

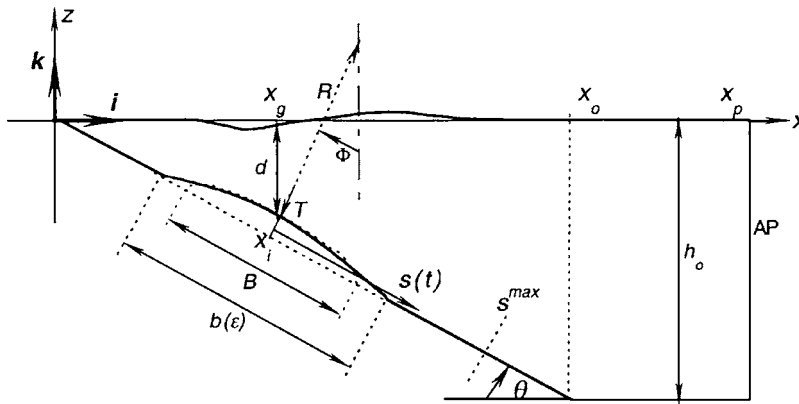


Fig. 1. Sketch of SMF tsunami problem geometry, main parameters, and setup of computational domain for 2D-FNPF numerical model

In most of the following analyses, we perform parametric studies of 2D tsunamis generated by SMFs of identical  $\epsilon$  values and, for comparison with earlier work,  $B$  rather than  $b$  is used as the horizontal landslide scale of reference. From Eq. (2), the actual SMF length is given by  $b=BC/C'$ .

### Numerical Methods

The computational domain used for applying GW's model is depicted in Fig. 1. The domain boundary is discretized by nodes; third-order spline elements are used to interpolate between nodes on the free surface and second-order isoparametric elements are used on the other boundaries. Unlike in GW, outgoing tsunamis are radiated out of the computational domain through the offshore boundary, by specifying the absorbing piston condition developed by Grilli and Horrillo in 1997 (AP; see Fig. 1). This allows us to perform longer term computations, in a shorter domain, without being limited by reflection at the offshore boundary.

Fully nonlinear kinematic and dynamic boundary conditions are specified on the free surface. These are time integrated using second-order explicit Taylor series expansions expressed in Lagrangian form, for both  $\phi$  and the free surface node positions. The time step  $\Delta t$  used in these series is adaptively specified based on a constant mesh Courant number and the minimum distance between two nodes on the free surface [see Grilli et al. (1989) and Grilli and Subramanya (1996) for details of numerical methods].

SMF geometry [Eqs. (1) and (2)] and kinematics are specified along the plane slope, as required for each specific application. In GW's landslide tsunami computations, to avoid singularities in the BEM, the use of semielliptical SMF geometry required both rounding off the  $90^\circ$  corners on each side of the SMF intersection with the slope and refining the discretization in these areas. Moreover, the discretization was assumed to move with the SMF, and mesh regridding was performed both behind and ahead of the SMF on the slope, which required very much reducing the time

step. In the present case, the SMF, represented according to Eq. (1), is simply specified as a "wave" of bottom elevation moving down the slope, with no node being linked to it. Hence, no refinement of the discretization is necessary and this procedure also does not affect time step, making the present computations much more efficient than those performed in GWs.

### SMF Boundary Conditions

According to Watts (1998, 2000), tsunami amplitudes scale with the center of mass motion. In the model, we specify the center of mass motion of underwater slides and slumps of given shape, parallel to the plane slope. These motions are detailed in the next section.

Due to the second-order time integration scheme, both normal flow velocity and acceleration must be specified as boundary conditions along the SMF. Following Grilli (1997) and GW, these conditions take the form

$$\frac{\partial \phi}{\partial n} = \mathbf{u}_\ell \cdot \mathbf{n}$$

and

$$\frac{\partial^2 \phi}{\partial t \partial n} = (\mathbf{a}_\ell \cdot \mathbf{n}) - (\mathbf{u}_\ell \cdot \mathbf{s}) \left( \frac{\partial^2 \phi}{\partial s \partial n} + \nu \frac{\partial \phi}{\partial s} \right) + \frac{\partial \phi}{\partial n} \left( \frac{\partial^2 \phi}{\partial s^2} - \nu \frac{\partial \phi}{\partial n} \right) \quad (3)$$

in which  $\mathbf{u}_\ell$  and  $\mathbf{a}_\ell$ =absolute SMF velocity and acceleration, respectively;  $\mathbf{n}$ =outward unit normal vector along the domain boundary;  $\mathbf{s}$ =corresponding tangential vector; and  $\nu = \zeta_{\xi\xi} / (1 + \zeta_\xi^2)^{3/2}$  is the SMF curvature (where subscripts denote partial derivative with respect to  $\xi$ ).

We represent the motion of rigid SMFs by the displacement  $S(t)$  of their center of mass parallel to the plane slope (Fig. 1). Detailed expressions for  $S$  are derived in the next sections for slides and slumps, as a function of the governing parameters. We also solve problems for slides with expanding length during their motion, while keeping a constant thickness; thus,  $B(t)$  may be a specified function of time. During such expansion, we may also assume that a uniform water flux, of normal velocity  $U$ , enters the slide to compensate for its volumetric expansion. Thus, based on the preceding geometric definitions

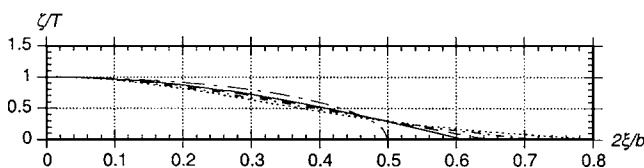


Fig. 2. SMF cross-section geometry specified in 2D model (only half is shown): ellipse ( $B/2, T$ ) (—) and Gaussian ( $b(\epsilon)/2, T$ ) with  $\epsilon=0.75$  (---),  $0.50$  (---),  $0.25$  (-·-·-), and  $0.10$  (----)

$$U = \frac{\pi(B - B_o)T}{4 \Delta t \ell} \text{ and } U = \frac{\pi T}{4 \Delta t \ell} \dot{B} \quad (4)$$

where  $B_o = B(0)$ ;  $\ell = \int_{-b/2}^{b/2} (1 + \zeta_\xi^2)^{1/2} d\xi$  denotes the arclength of the slide; and the upper dot indicates absolute time derivative.

Therefore, we represent the SMF geometry in axes  $(x, z)$  of unit vectors  $(\mathbf{i}, \mathbf{k})$  as

$$\mathbf{x}_\ell = \{x_i + (S + \xi)\cos \theta + \zeta \sin \theta\}\mathbf{i} + \{z_i - (S + \xi)\sin \theta + \zeta \cos \theta\}\mathbf{k} \quad (5)$$

in which  $\mathbf{x}_i = (x_i, z_i)$  denotes the initial SMF axes origin on the slope

$$\mathbf{x}_i = (d + T \cos \theta) \left( \frac{1}{\tan \theta} \mathbf{i} - \mathbf{k} \right) \quad (6)$$

with  $\xi \in [-b/2, b/2]$ . Using Eq. (5), SMF velocity is defined as

$$\mathbf{u}_\ell = \{\dot{S} \cos \theta + \dot{\zeta} \sin \theta\}\mathbf{i} + \{\dot{\zeta} \cos \theta - \dot{S} \sin \theta\}\mathbf{i} \quad (7)$$

with a similar expression for  $\mathbf{a}_\ell$ , involving second-order time derivatives.

From Eq. (1), we have  $\dot{\zeta} = -\xi \zeta_\xi \dot{B}/B$ , and we find the SMF motion terms in Eqs. (3) as

$$\mathbf{u}_\ell \cdot \mathbf{n} = \left( \dot{S} + \xi \frac{\dot{B}}{B} \right) \sin \alpha + U$$

$$\mathbf{u}_\ell \cdot \mathbf{s} = \left( -\dot{S} + \xi \zeta_\xi^2 \frac{\dot{B}}{B} \right) \cos \alpha$$

$$\mathbf{a}_\ell \cdot \mathbf{n} = \left( \ddot{S} - \xi \left\{ \frac{\zeta_{\xi\xi\xi}}{\zeta_\xi} \xi + 2 \right\} \left( \frac{\dot{B}}{B} \right)^2 - \frac{\ddot{B}}{B} \right) \sin \alpha + \dot{U} \quad (8)$$

with the definition  $\zeta_\xi = \tan \alpha$ .

## Presentation of Results

SMF tsunamis computed with the model will be represented either by their free surface elevation as a function of space at some time  $t_c, \eta(x, t_c)$ , or by their elevation at fixed locations  $x_c$  as a function of time,  $\eta(x_c, t)$ . The latter representation is the equivalent of a “numerical wave gauge” (or gauge), such as used in laboratory experiments.

To characterize the intensity of the generated tsunamis, we will use a single free surface elevation,  $\eta_o$ , defined as the maximum draw down, or depression, calculated at a gauge located above the SMF initial submergence location,  $x_g = d/\tan \theta + T/\sin \theta$  (Fig. 1), i.e.,  $\eta_o = a = |\text{MIN}(\eta(x_g, t))|$ . The use of this 2D characteristic tsunami amplitude may appear arbitrary, but it originates in the experimental work of Watts (1998) and is the measure of tsunami amplitude least contaminated by the surrounding bottom topography. We will show that many useful results, such as coastal runup  $R_w$ , can be simply expressed as a function of  $\eta_o$ .

## SMF Types and Kinematics

The motion of the outer boundary of the SMF down the slope is expressed by Eqs. (3)–(8) in numerical simulations. As for any mechanical system, these equations describe the center of mass motion, combined with deformation with respect to the center of mass. We detail results for two idealized SMF types: underwater

slides and slumps. In applications, we mostly assume negligible SMF deformation during motion. Deformation effects on tsunami shape are separately estimated for underwater slides.

For both SMF types, we will derive a characteristic time of motion  $t_o$  as a function of governing parameters. The corresponding characteristic tsunami wavelength can be expressed as

$$\lambda_o = t_o \sqrt{gd} \quad (9)$$

and used as a representative measure of the horizontal extension of the generated tsunami (Watts 1998, 2000).

Slides typically have low basal Coulomb friction once the motion is initiated, which yields a terminal velocity that is essentially limited by hydrodynamic drag (both form and skin friction) and the length of the slope. [Dobry et al. (1982) and Seed et al. (1988) show that sand and silt can experience a drop in shear stress by up to an order of magnitude during slope failure, thereby justifying neglect of a frictional force for slides.] By the time the slide comes to rest within some oceanic deep, considerable deformation may have occurred, or a turbidity current may have formed (Lee et al. 1991). On the other hand, the rotation of a cohesive slump is retarded by significant basal friction that can keep slump velocity from reaching large values and thus fluid dynamic drag from reaching important scales. While a slump does not usually travel very far before coming to rest, it may break into distinct blocks that experience significant relative motion (Lee et al. 1991).

In the following sections, we derive the center of mass motion  $S$  parallel to a plane slope of underwater slides and slumps, of geometry described by Eq. (1) (Fig. 1). While we assume idealized SMF shape and failure surfaces, experimental and numerical work indicates that these only need to remain valid during the early times  $t < t_o$ , when tsunami generation is most intense, in order for the computed tsunami amplitudes to be realistic (Watts 1997; Watts and Grilli 2003; Watts et al. 2003). This small time constraint is easily achievable in many practical situations and explains the success of case studies conducted this way (see Part II for detail).

We model a slump as a rigid body rotating a small angle  $\Delta\Phi = \Phi_f - \Phi_i$ , along a circular arc of radius  $R$  (failure plane), where  $\Phi_f$  and  $\Phi_i$  denote the initial and final center of mass angles in radians, respectively, (Fig. 1). Due to the small  $\Delta\Phi$ , a slump motion is also approximated in the model by its center of mass translation parallel to the slope,  $S \approx R(\Phi - \Phi_i)$ . The error incurred by approximating the arc by the chord is roughly  $R(\Delta\Phi)^2/2$ , which is negligible in most applications, given the limited angular displacement of slumps. For example, we estimate the maximum spatial error resulting from this approximation to be around 5% of the maximum slump thickness in the case of the 1998 Papua New Guinea slump (see Part II).

## Governing Equation for SMF Center of Mass Motion

Dimensional analysis shows that, within a family of similar SMF cross sections, with characteristic length  $B$ , width  $w$ , and thickness  $T$  (Fig. 1), SMF motion and generated tsunami characteristics can be expressed as functions of seven nondimensional independent parameters: (1) relative SMF density  $\gamma = \rho_\ell / \rho_w$  (where  $\rho_\ell$  and  $\rho_w$  denote SMF bulk and water density, respectively); (2) slope angle  $\theta$ ; (3) basal Coulomb friction coefficient  $C_n = \tan \psi$ ; (4) hydrodynamic added mass coefficient  $C_m$ ; (5) global hydrodynamic drag coefficient  $C_d$  (including form and friction drag, which both scale with surface area); (6) relative SMF submergence depth  $d/B$ ; and (7) relative SMF thickness  $T/B$ .

Assuming a rigid SMF and expressing Newton's first law of motion, a differential equation can be derived, describing center of mass motion  $S(t)$ , parallel to the slope. Thus, balancing inertia, gravity, buoyancy, basal Coulomb friction, and hydrodynamic drag forces, we find (upper dots denote time derivatives):

$$(M_\ell + \Delta M_\ell)\ddot{S} = (M_\ell - \rho_w V_\ell)(\sin \theta - C_n \cos \theta)g - \frac{1}{2}\rho_w C_d A_c \dot{S}^2 \quad (10)$$

where  $g$ =gravitational acceleration;  $\Delta M_\ell$  and  $A_c = Tw$  are the SMF added mass and main cross section perpendicular to the direction of motion, respectively. Eq. (10) can be further simplified into

$$(\gamma + C_m)\ddot{S} = (\gamma - 1)(\sin \theta - C_n \cos \theta)g - C_d \frac{2}{\pi B} \dot{S}^2 \quad (11)$$

where  $C_m = \Delta M_\ell / (\rho_w V_\ell)$  is mostly a function of SMF shape. [Watts (2000) also shows a weak dependence of  $C_m$  on submergence  $d$ .] For high Reynolds number flows,  $C_d$  is assumed to depend on SMF shape only and provides dissipation in Eq. (11), even if, e.g., for slides,  $C_n \approx 0$ .

### Slide Center of Mass Motion

Integrating Eq. (11) for slides starting at rest at time  $t=0$ , with  $S=0$  and  $\dot{S}=0$ , we find

$$S(t) = S_o \ln \left( \cosh \frac{t}{t_o} \right) \quad (12)$$

with the characteristic distance and time of motion

$$S_o = \frac{u_t^2}{a_o} \quad \text{and} \quad t_o = \frac{u_t}{a_o} \quad (13)$$

respectively, where  $a_o = \ddot{S}(0)$  is the slide initial acceleration; and  $u_t = \dot{S}(\infty)$  (with  $\ddot{S}(\infty)=0$ ) is the terminal velocity for large times, defined as

$$a_o = g \sin \theta \left( \frac{\gamma - 1}{\gamma + C_m} \right) \left( 1 - \frac{\tan \psi}{\tan \theta} \right) \quad (14)$$

and

$$u_t = \sqrt{gd} \sqrt{\frac{B \sin \theta \pi (\gamma - 1)}{d} \left( 1 - \frac{\tan \psi}{\tan \theta} \right)} \quad (15)$$

respectively. Based on Eq. (12), the velocity and acceleration of the slide center of mass are

$$\dot{S} = u_t \tanh \left( \frac{t}{t_o} \right) \quad \text{and} \quad \ddot{S} = a_o \cosh^{-2} \left( \frac{t}{t_o} \right) \quad (16)$$

respectively.

The first term in the Taylor series expansion of Eq. (12) about  $t=0$  is  $a_o t^2/2$ , as required for a body accelerating from a state of rest. Eq. (13) shows that a unique characteristic distance and time exist for each underwater slide. We show in a following section that Eq. (12) closely matches the center of mass motion of a rigid slide measured in laboratory experiments. Watts (1997) and Watts and Grilli (2003), experimentally and numerically showed that the center of mass motion of deforming slides can also be accurately described by Eq. (12), until at least  $t \approx t_o$ . Hence, our results are robust, and changes in effective dynamical coefficients brought on by landslide deformation do not noticeably alter the center of

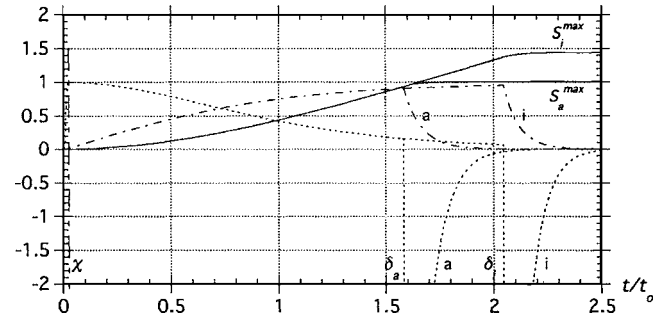


**Fig. 3.** Underwater slide kinematics specified in 2D model [Eqs. (12)–(16) and (24)–(28); Fig. 1], with  $\theta=15^\circ$ ,  $\gamma=1.85$ ,  $C_m=1$ ,  $C_d=1$ ,  $C_n=0$ ,  $h'_o=2$ ,  $T'=0.052$ ,  $\varepsilon=0.75$ ,  $\chi=0.02$ ,  $f=0.10$ , and  $d'=a:0.625$ ,  $i:0.125$ ;  $S/S_o$  (—),  $\dot{S}/u_t$  (---),  $\ddot{S}/a_o$  (— · —)

mass motion at short times. The center of mass motion at later times can become influenced by particle effects, including the bulk rotation of the landslide (Watts 1997).

Based on experimental work, appropriate values of the coefficients in Eqs. (14) and (15) are  $\psi \approx 0$ ,  $C_m \approx 1$ , and  $C_d \approx 1$  (Watts 1997, 1998; Watts et al. 2000; Grilli and Watts 2001; Enet et al. 2003). The latter two coefficients are similar to those of a circular cylinder. Based on the form of these equations, SMF motion is not highly sensitive to the precise values of the dynamical coefficients, particularly  $C_m$ . For any specified values of  $\gamma$ ,  $C_m$ , and  $C_d$ , Eqs. (13)–(15) show a strong dependence of center of mass motion on slide length and slope angle.

When using the 2D-FNPF model (Fig. 1), to avoid initial inaccuracies (singularities) in computations, the slide acceleration is gently ramped up to its value given by Eq. (16), over a small time interval  $t_i = \chi t_o$ , following a hyperbolic tangent variation. We will show that a similar ramp-up is also observed in laboratory experiments. [In fact, around  $t \approx 0$ , both velocity and Reynolds number are very low, and viscosity should affect slide motion and cause the initial ramp-up (Watts 1997).] Moreover, because the slope has a finite length  $h_o/\tan \theta$  in the computational domain, the slide must be decelerated at some distance from the toe of the slope ( $x_o, -h_o$ ), say, for  $t > \delta t_o$ , in order for its forward edge to come to a rest at this location. Fig. 3 shows two examples of the actual slide law of motion specified in the computational model, for two initial slide submergences, with both ramp-up and deceleration. Details of the corresponding equations are given in the Appendix.

### Slump Center of Mass Motion

For slumps, shear stress  $S_u$  along the failure plane may be assumed to remain constant during motion (Bardet 1997). Defining  $A_b = wb$ , the area of the failure plane projected on the slope, we find

$$C_n = S_u \frac{4b}{\pi B (\rho_\ell - \rho_w) T_g \cos \theta} \quad (17)$$

with  $b/B = C/C'$  a function of  $\varepsilon$ . Due to the small angular rotation of slumps, the influence of fluid dynamic drag and angular non-linearity on center of the mass motion are often negligible [these effects could be evaluated from the exact solution of a damped oscillator; e.g., Nayfeh and Mook (1979)]. Hence, specifying  $C_d \approx 0$ ,  $S = R(\Phi - \Phi_i)$  and  $\sin \theta \approx -\sin \Phi \approx -\Phi$ , the linearized Eq. (11) becomes

$$t_o^2 \ddot{\Phi} + \Phi = C_n \cos \theta \quad (18)$$

which, for slumps starting at rest with  $\Phi = \Phi_i$  and  $\dot{\Phi} = 0$  at time  $t = 0$ , yields

$$S(t) = S_o \left( 1 - \cos \frac{t}{t_o} \right) \quad (19)$$

with the characteristic distance and time of motion

$$S_o = \frac{R \Delta \Phi}{2} = R C_n \cos \theta \quad \text{and} \quad t_o = \sqrt{\frac{R}{g}} \sqrt{\frac{\gamma + C_m}{\gamma - 1}} \quad (20)$$

respectively. Based on Eq. (19), the velocity and acceleration of the slump center of mass are

$$\dot{S} = \frac{S_o}{t_o} \sin \left( \frac{t}{t_o} \right) \quad \text{and} \quad \ddot{S} = a_o \cos \left( \frac{t}{t_o} \right) \quad (21)$$

respectively, where  $a_o = \ddot{S}(0) = S_o/t_o^2$  is the slump initial acceleration.

As does Eq. (12), Eq. (19) appears in the form  $S/S_o = \mathcal{F}(t/t_o)$ , with unique characteristic distance and time of slump motion. The latter, given by Eq. (20), is found in accordance with the period of pendular motion. The slump thus reaches a maximum velocity  $u_{max} = S_o/t_o$  at the middle of its motion, for  $t = \pi t_o/2$  [Eq. (21)], before coming to a halt at  $t = \pi t_o$ , with  $S = 2S_o$ . The first term in the Taylor series expansion of Eq. (19) about  $t = 0$  is also  $a_o t^2/2$ , although the physical parameters that determine the initial acceleration differ from those of a slide. Due to linearization, neglect of the fluid dynamic drag, and the assumption of a circular failure plan, the slump motion described here must be considered approximate. As for slide, we also specify a ramp-up and, if necessary, a deceleration of slump motion to account for the finite length of the slope. Modified equations are given in the Appendix.

In case studies, the value of  $S_o$  in Eq. (20) may be fixed by observations of slump center of mass motion, yielding information on a characteristic shear strength along the failure plane [Eq. (17)]. The fact that the characteristic distance of motion is proportional to shear strength raises an apparent paradox that we resolve in Part II of this work. Because  $t_o$  in Eq. (20) is fairly insensitive to  $\gamma$ , observations of tsunami period suffice in general to estimate a radius of curvature and, based on the geology, bolster (or refute) classification of an SMF as an underwater slump. We note that, for specified values of  $\gamma$  and  $C_m$ , center of mass motion strongly depends on the radius of curvature, and not on any explicit measure of slump size (a well-known property of a pendulum).

## Numerical Simulations and Sensitivity Analyses

Numerical simulations are performed to validate our model by comparing results to laboratory experiments and to quantify effects of governing parameters on SMF tsunami amplitude and coastal runup. In each case, BEM discretizations and time steps are selected to provide high accuracy of numerical results. For any given time step, the relative error on mass conservation is usually on the order of  $10^{-9}$ . Numbers of time steps typically vary between 1,000 and 2,300 and the integrated error on mass conservation (which includes both BEM solution and time stepping) in the computational domain is usually much less than 0.01% at the end of computations. In all the numerical simulations in this section, we scale geometric dimensions by the SMF characteristic

length  $B$  and indicate the nondimensional variables by a prime. We select constant values of  $\gamma = 1.85$  and the dynamic coefficients  $C_m = 1, C_d = 1$  for slides and  $C_d = 0$  for slumps. We assume  $C_n = 0$  for slides, except when comparing results to laboratory experiments, and nonzero values for slumps. For the ramp-up and deceleration of both slide and slump motion, we use  $\chi = 0.02$  and  $f = 0.1$  (see Appendix).

We first analyze the effects of SMF shape spreading parameter  $\varepsilon$  and domain depth on tsunamis generated by slides. In subsequent simulations and sensitivity analyses,  $\varepsilon$  is maintained constant at 0.75. In sensitivity analyses in Parts I and II, we vary the computational domain geometry (i.e., slope angle  $\theta$ , domain depth  $h'_o$ , and length  $x'_p$ ), the initial depth  $d'$ , thickness  $T'$ , and specific density  $\gamma$ . We estimate effects of SMF deformation for slides over three different slopes. We then show differences between tsunamis generated by underwater slides and slumps and, finally, study in detail the effect of slide submergence depth on generated tsunami features and runup for one slope.

For data reduction and analyses, it is convenient to introduce a reference depth  $d_{ref} = B \sin \theta$ , which represents the SMF initial vertical extension on the slope. Watts (2000) showed that nonlinearity of the generated tsunami grows with  $d_{ref}/d$  [which in fact appears in Eq. (15)]. We also introduce a reference thickness  $T_{ref} = 0.2d_{ref}$ , and a reference density  $\gamma_{ref} = 1.85$ , which both may represent typical values for SMFs. It follows from Eq. (2) that  $V'_{lref} = \pi T'_{ref}/4$ .

### Effects of Shape Spreading and Domain Depth for Rigid Slides

We simulate tsunami generation by a slide over a slope of angle  $\theta = 15^\circ$ . We select  $T' = T'_{ref} = 0.052$ ,  $d' = d'_{ref} = 0.259$ ,  $h'_o = 1$ , and a domain length  $x'_p = 10$ . With  $C_m = C_d = 1$  and  $C_n = 0$ , Eqs. (12)–(15) yield  $S'_o = 4.477$ ,  $t'_o = 7.615$ , and  $\lambda'_o = 3.876$ . We perform four simulations for  $\varepsilon = 0.1, 0.25, 0.50$ , and  $0.75$  (see slide shapes in Fig. 2) and calculate tsunami amplitude at gauges located at  $x'_g = 1.168$  and  $x' = 4$  (which is beyond the toe of the slope at  $x'_o = 3.732$ ) and coastal runup  $R'$ , defined as the vertical elevation of the moving shoreline.

In Fig. 4(a), in all cases, we first see a drawdown at  $x_g$  that reaches a maximum for  $t \approx 0.5t_o$ , followed by a slightly smaller “rebound” elevation wave. The characteristic amplitude (maximum drawdown) is the largest for  $\varepsilon = 0.75$ , with  $\eta'_o \approx 0.008$ . In Fig. 4(b) we see that the outgoing tsunami at  $x' = 4$  is also the largest in the latter case. In Fig. 4(c), at the shoreline, we first observe a rundown, for  $t' \approx 0.6t_o$ , which also increases with  $\varepsilon$ , followed by a runup of similar amplitude, which does not seem affected by  $\varepsilon$ . Hence, as could have been expected, the most compact slide, with the largest  $\varepsilon = 0.75$ , produces both the largest tsunami and coastal effects. Applying the model to a semielliptical slide, as in GW, would have produced results close to those obtained for  $\varepsilon = 0.75$  ( $\eta'_o = 0.009$  see Part II). This justifies using semielliptical or nearly semielliptical slides to produce worst case tsunami scenarios for characteristic amplitude, outgoing tsunami, and runup in this idealized domain geometry. Thus, in subsequent computations in Part I, we use  $\varepsilon = 0.75$ .

Similar computations are repeated in a following section for  $\varepsilon = 0.75$ , but with a larger domain depth  $h'_o = 2$  and hence a longer slope and time of slide motion before deceleration (Fig. 12 curve e). In this case, we see that the characteristic amplitude only slightly increases to  $\eta'_o = 0.0084$ , and the outgoing tsunami amplitude increases proportionally. Coastal runup, however, is decreased, from  $R'_u = 0.015$  [in Fig. 4(c)] to about 0.012, while run-

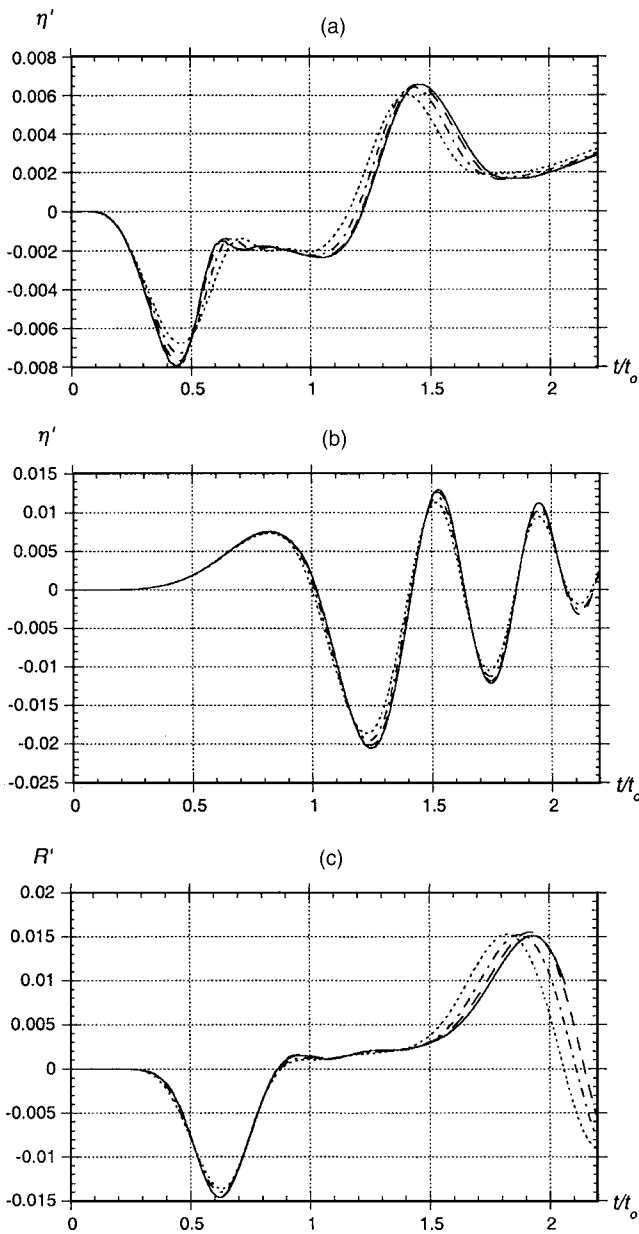


**Fig. 4.** Tsunami sensitivity to SMF shape, for slide with  $\theta=15^\circ$ ,  $\gamma=1.85$ ,  $C_m=1$ ,  $C_d=1$ ,  $C_n=0$ ,  $h'_o=1$ ,  $T'=0.052$ ,  $d'=0.259$ ,  $\chi=0.02$ ,  $f=0.010$ , and  $\varepsilon=0.10$  to  $0.75$ . Curves are defined as in Fig. 2, and: (a) gauge elevation at  $x'_g=1.168$ ; (b) gauge elevation at  $x'_g=4$ ; and (c) coastal runup.

down is unaffected. The same trend is observed for all the other submergence depths considered in this work ( $d'=0.125$  to  $0.625$ ; results for  $h'_o=1$  are not shown). The persistence of rundown results for different slope length is to be expected, because rundown is created by the drawdown caused by initial slide motion. The decrease in runup for a longer slope can be explained by the weaker runup-producing rebound wave that occurs, as a result of the delayed slide deceleration in deeper water, as compared to the present case.

To be able to test slides starting in deeper water and/or having a large deformation, all subsequent computations are performed in a domain of depth  $h'_o=2$ . As seen previously, for rigid slides, this will not affect  $\eta'_o$  or the outgoing tsunami very much. Coastal

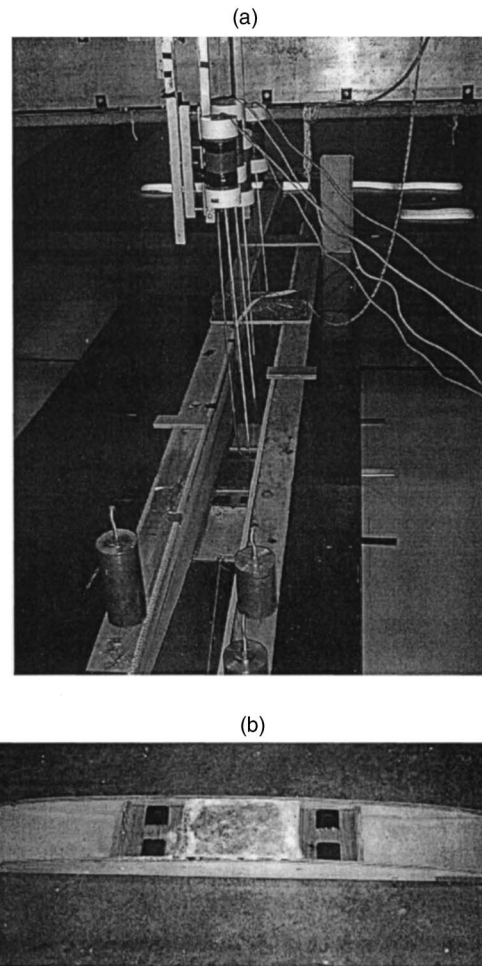


**Fig. 5.** Laboratory experiments for 2D slide over  $\theta=15^\circ$  slope: (a) experimental setup for submergence depth  $d=d_{ref}=0.259$  m, with four capacitance wave gauges; and (b) semielliptical plywood and mylar slide model with  $B=1$  m,  $T=T_{ref}=0.052$  m,  $w=0.2$  m, and lead weight (at center) to achieve  $\gamma=1.806$

runup, however, could be increased in a shallower domain. This detailed analysis of runup will be left out for further studies.

### Validation with Laboratory Experiments for Rigid Slides

The 2D-FNPF model used in these simulations has been extensively validated for long wave generation by wavemakers, propagation, shoaling, and breaking over plane slopes, by comparing numerical results with measurements in precision laboratory wave tanks (Grilli et al. 1994; Grilli et al. 1997, 1998). Such comparisons, for instance, showed that solitary wave shapes at and during breaking over slopes could be simulated in the model to within 1% of experimental values.

In order to specifically validate the model for the generation of SMF tsunamis, particularly when using the geometric and kinematic models discussed earlier, 2D experiments were conducted in a 30-m-long, 3.7-m-wide, and 1.8-m-deep wave tank at the University of Rhode Island [Fig. 5(a)]. The tank was equipped with a segmented aluminum beach with adjustable slope. Two 2.4-m-long beach segments were set to a  $\theta=15^\circ$  angle in water  $h_o=1.05$  m deep. In order to have a very smooth sliding surface, an aluminum plate was placed on the beach. To simulate a 2D

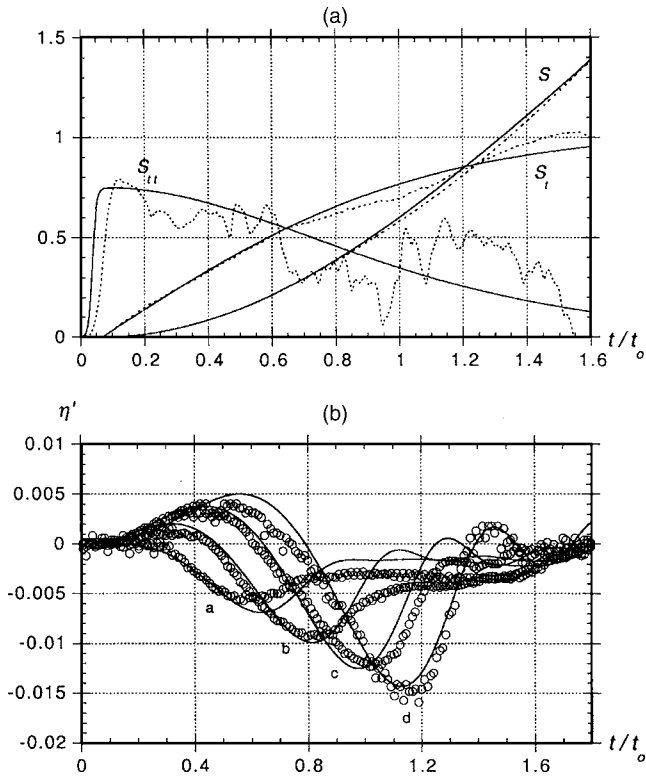


**Fig. 6.** Results of laboratory experiments (○) (---) and simulations (—), for 2D slide experiments of Fig. 5): (a) slide kinematics; and (b) elevation  $\eta'$  at gauges located at  $x'=a:1.175$ ,  $b:1.475$ ,  $c:1.775$ ,  $d:2.075$

geometry, two plywood sidewalls were installed, 20 cm apart from each other, near the center of the tank. A semielliptical slide model [Fig. 5(b)] was built out of plywood and mylar sheets. Melted lead was poured in a central cavity in the model, in order to achieve an average density  $\gamma=1.806$  in the fresh water tank, corresponding to  $\rho_\ell=1,850 \text{ kg/m}^3$  in sea water of density  $\rho_w=1,025 \text{ kg/m}^3$ . The model dimensions were length  $B=1 \text{ m}$ , thickness  $T=T_{ref}=0.052 \text{ m}$ , and width  $w=0.2 \text{ m}$ . Four plastic wheels, with water-sealed bearings, were installed at the bottom part of the model (black cylinders in the picture), to provide for a smooth sliding down the slope, as frictionless as possible, about 2 mm above the slope. A microaccelerometer was embedded at the model center of mass and inclined perpendicular to the slope, with its controlling cable exiting through the back of the model in order to record center of mass acceleration during experiments. Four capacitance wave gauges were installed at locations  $x=1.175, 1.475, 1.775, 2.075 \text{ m}$ , the first location being identical to  $x_g$  (Fig. 1). Due to the small magnitude of the measured amplitudes (millimeters), the gauge wires were coated with a polymer aimed at reducing meniscus effects. A multichannel, 100 Hz data acquisition system was used to record measurements from the gauges and the accelerometer on a personal computer. In experiments, the model was first located at its initial submergence depth under the first gauge and maintained in position by a cable, the data acquisition system was started, and the cable was released.

Fig. 6(a) shows a typical slide acceleration, noted  $S_{tt}$ , measured for  $d=d_{ref}=0.259$  and filtered to remove high frequency oscillations. The raw acceleration was integrated to obtain velocity  $S_t$ , and integrated again to yield center of mass motion  $S$ . Slide

motion was found to be highly repeatable in experiments, particularly for early time, despite fluctuations in the filtered acceleration and corresponding velocity, likely due to small shocks between the model and the sidewalls. The slide law of motion [Eqs. (12)–(16), with the ramp-up represented by Eq. (24)] was curve-fitted to experimental measurements [see Fig. 6(a)]. The initial acceleration after ramp-up  $a_i$  and ramp-up time  $t_i$  were obtained from the acceleration measurements. The terminal velocity  $u_t$  was then found by least square fitting of the theoretical equation for  $S$  to the twice integrated data. Eq. (13) then provided  $t_o$  and  $S_o$ , and Eqs. (14) and (15) provided  $C_m$  and  $C_d$ . For one trial with  $d=d_{ref}=0.259$ , for instance, we obtained  $a_i=0.750 \text{ m/s}^2$ ,  $t_i=0.09 \text{ s}$ ,  $u_t=1.258 \text{ m/s}$ ,  $t_o=1.677 \text{ s}$ ,  $C_m=0.923$ , and  $C_d=2.031$  (with  $C_n=0$ ). We thus find  $C_m$  close to the expected theoretical value;  $C_d$  is larger than expected, likely due to sidewall friction. Assuming  $C_n=0.136$  in Eq. (15), for instance, would yield  $C_d=1$ .

The curve-fitted slide kinematics was used in the 2D-FNPF model to simulate experiments for  $d=d_{ref}=0.259$ . The model geometry was specified to closely match that of experiments. For better accuracy and efficiency in computations, we used a Gaussian geometry with  $\varepsilon=0.75$  (Fig. 2), which should produce results quite close to those of a semielliptical slide, as discussed in the previous section. Simulated and measured data at the four gauges are shown in Fig. 6(b) as a function of time. We see a good overall agreement between these. Some discrepancies can be seen after drawdown in the first two gauges, a and b. However, the back of the tsunami wave measured further downstream at the fourth gauge, d, agrees well with experiments. Hence, the small discrepancies mentioned could be due to unwanted surface tension effects. Measurements at the gauges were found to be well repeatable, except for small differences in the smaller oscillations.

In view of this comparison, and considering the experimental variations and errors inherent to laboratory work and data processing, it can be concluded that the 2D-FNPF model used here was successfully validated by these 2D rigid slide experiments.

### Effects of Mass Failure Deformation for Slides

Watts and Grilli (2003) simulated deformable underwater slides using a modified Bingham model. Results showed that the center of mass motion of such slides is still accurately described by Eq. (12) and that the primary mode of deformation is an extension along the slope, in response to the center of mass motion, with a secondary reduction of slide thickness. This mode of deformation was also observed in Watts' (1997) experiments with a granular sliding mass.

To investigate the impact of SMF deformation on tsunami features, we return to the previous underwater slide case, with  $\theta=15^\circ$ ,  $\gamma=1.85$ ,  $T'=T'_{ref}=0.052$ ,  $d'=d'_{ref}=0.259$ , and  $\varepsilon=0.75$ , and perform numerical simulations with an expanding slide length given by  $b(t)=B(t)C/C'$ , where

$$B = B_o \{1 + \Gamma t(1 - e^{-k_\Gamma t})\}$$

$$\dot{B} = B_o \Gamma \{1 - (1 - k_\Gamma t)e^{-k_\Gamma t}\}$$

$$\ddot{B} = B_o \Gamma k_\Gamma e^{-k_\Gamma t} (2 - k_\Gamma t) \quad (22)$$

with  $b_o=B_o C/C'$ , the initial slide length and  $\Gamma$  the slide rate of extension. Coefficient  $k_\Gamma = -\ln \varepsilon_\Gamma / (\delta_\Gamma t_o)$  is selected to produce an initial transient, ramping up the slide rate of extension to  $(1 - \varepsilon_\Gamma)\Gamma$  over a specified time interval  $\delta_\Gamma t_o$ . In the following com-

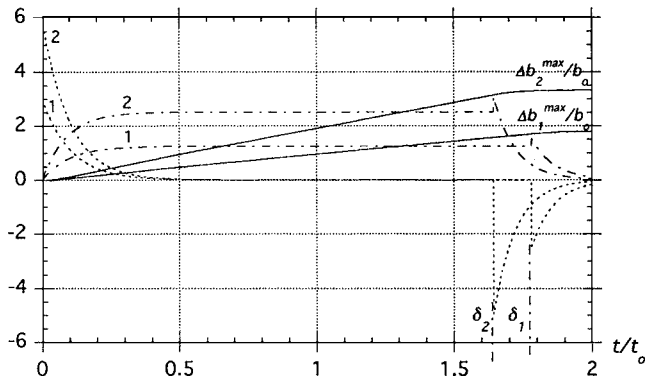


**Fig. 7.** Tsunami sensitivity to SMF deformation, for slide with  $\theta=15^\circ$ ,  $\gamma=1.85$ ,  $C_m=1$ ,  $C_d=1$ ,  $C_n=0$ ,  $h'_o=2$ ,  $T'=0.052$ ,  $d'=0.259$ ,  $\chi=0.02$ ,  $f=0.10$ , and  $\varepsilon=0.75$ . Slide deformation:  $B/B_o$  (—),  $(10\times)\dot{B}/B_o$  (---),  $(10\times)\ddot{B}/B_o$  (- - - -), for  $\Gamma\sqrt{B_o/g}=(1)$  0.125; (2) 0.250.

putations, we arbitrarily selected  $\varepsilon_\Gamma=0.01$  and  $\delta_\Gamma=0.5$ . More realistic values could be obtained from Watts' (1997) or Watts and Grilli's (2003) results. When the slide approaches the bottom of the slope in the model and enters the deceleration region [described by Eqs. (26) and (28) in the Appendix; Fig. 3], we also specify a progressive reduction of the extension rate, in order for slide length to reach a constant value  $b(t^{max})$  when the slide comes to a rest. Modified equations used for  $B(t)$  and its derivatives are given in the Appendix [Eq. (31)], and Fig. 7 shows two examples of  $B(t)$ , described by Eq. (22) from  $t=0$  to  $\delta t_o$ , and then having an extension rate reduction specified for  $t>\delta t_o$ . Eq. (22) [and Eq. (31)] is used together with Eqs. (3)–(8) to specify bound-

ary conditions in the model, along the expanding slide boundary. As a first approximation, in these simulations, slide thickness is maintained constant during the expansion. This assumption produces stronger tsunamis and is thus on the conservative side.

To compensate for the slide volumetric expansion and prevent the creation of slide mass, we also specify a positive uniform normal velocity  $U$  along the slide boundary, calculated at each time step from Eq. (4), based on the instantaneous slide geometry and volume change due to slide expansion. Both  $U$  and  $\dot{U}$  are specified in boundary conditions Eq. (8). Note that the expanding slide bulk density should in fact be gradually reduced and the center of mass motion slowed down, due to water entering the slide outer regions. This effect, which would also reduce tsunami generation, is neglected as well in the present simulations.

An upper bound value for the rate of extension can be inferred from Watts and Grilli's (2003) computations (their Fig. 7). It was found that a highly deformable slide, with  $\gamma=1.85$ , reached a length  $b\approx 3.3b_o$  on a  $5^\circ$  slope, for  $t\approx 1.41t_o$ , i.e., a fairly large time for tsunami generation. Using Eqs. (12)–(16) with  $C_m=C_d=1$  and  $C_n=0$ , we find  $t_o\approx 3.9\sqrt{B_o/g}/(g\sin\theta)$ . In Eq. (22), the rate of extension tends to  $(B/B_o-1)/t$  for large time, with  $B/B_o=b/b_o$ . Hence, based on the preceding we get  $\Gamma_{max}\approx 0.42\sqrt{g\sin\theta/B_o}$ , or  $\Gamma_{max}\sqrt{B_o/g}\approx 0.21$  in the present case. In the following computations, we arbitrarily specify 20% more than this value, or 0.25, as the maximum dimensionless rate of extension; we also simulate an intermediate case with  $\Gamma\sqrt{B_o/g}=0.125$ . As usual, we compute wave elevation at a series of gauges, the first one being above the middle of the initial landslide position, at  $x=x_g$ . Fig. 8 shows results for three simulations, with  $\Gamma\sqrt{B_o/g}=0$  (i.e., rigid slide), 0.125, and 0.250 (de-

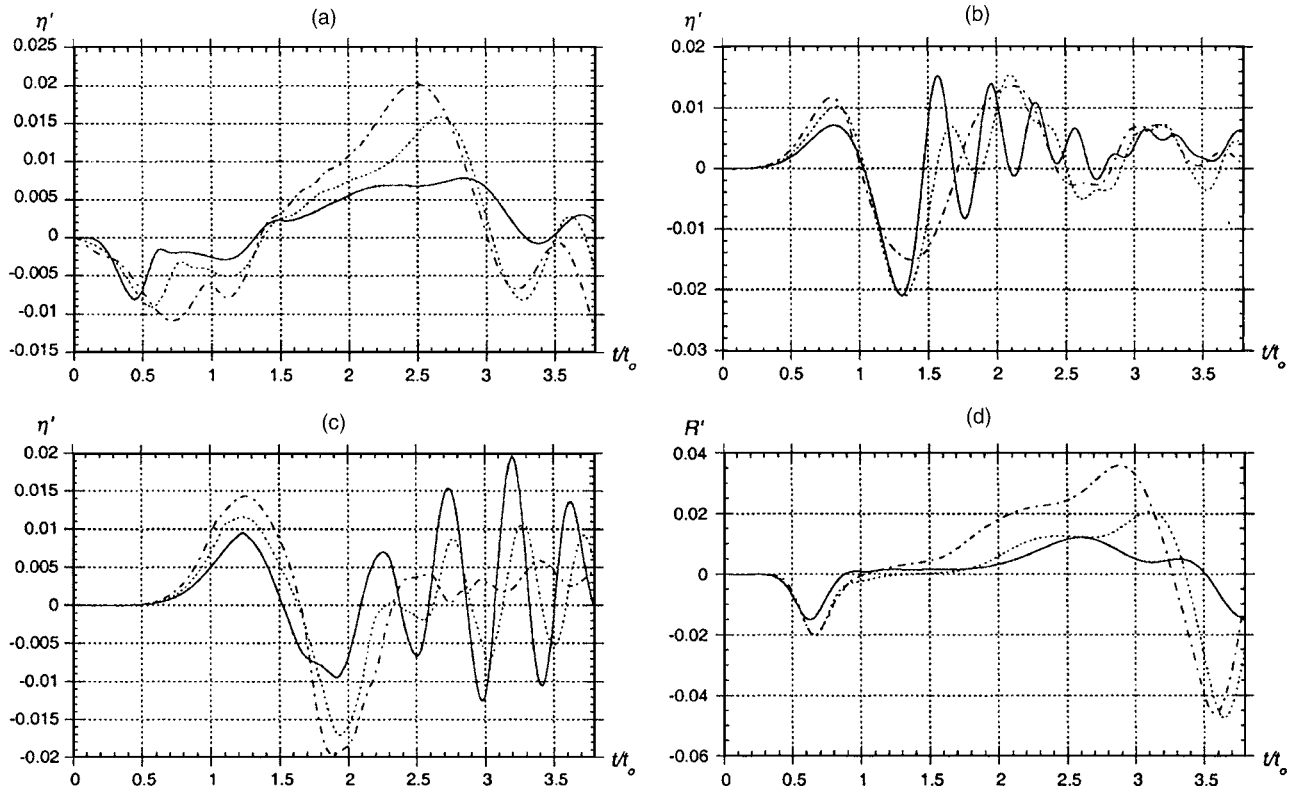


**Fig. 8.** Tsunami sensitivity to SMF deformation, for slide with parameters as in Fig. 7 and  $\Gamma\sqrt{B_o/g}=0$  (—), 0.125 (- - - -), and 0.250 (---): (a) gauge elevation at  $x'_g=1.168$ ; (b) gauge elevation at  $x'_g=4$ ; (c) gauge elevation at  $x'_g=7$ ; and (d) coastal runup

forming slides), respectively. Deformation for the latter two cases is given in Fig. 7 as a function of time, and we see that  $\Delta b^{max}/b_o = (b^{max} - b_o)/b_o$  (i.e., the incremental slide extension) reaches  $\approx 1.8$  and  $3.4$  at the end of slide motion, for each case, respectively.

For the gauge located at  $x = x_g$ , results in Fig. 8(a) show that the initial drop in wave amplitude is slightly faster when deformation is present and then proceeds more slowly at later times, as also noted by Watts et al. (2000). The characteristic tsunami amplitude  $\eta'_o$  of the deforming slides increases as compared to that of the rigid slide. This increase is moderate in the first deforming case, about 13%, but much more significant in the second case, at about 35%. The positive elevation wave occurring at  $x = x_g$  after the first drawdown is even more affected by deformation. This is to be expected, because it is generated at a later time, when deformation has had more time to affect tsunami shape, through the slide boundary conditions. As compared to the rigid slide, the positive amplitude increases by a factor of 2 in the first deforming case and 2.7 in the second case. The shape and amplitude of the outgoing tsunamis generated by the deforming slides (at  $x' = 4$  and  $7$ , respectively) are also quite different from those of the rigid slide [Figs. 8(b and c)]. Notably, it appears that deformation significantly affects wavelength and reduces dispersive effects. Whereas a well developed train of large dispersive waves follows a leading soliton-like wave in the rigid slide case, this dispersive train gradually disappears and tsunami wavelength increases as the slide extension rate increases. Fig. 8(d), finally, shows the effect of deformation on coastal runup. As could be expected, this effect is quite moderate on rundown (which is mostly a result of the initial drawdown). Runup, however, is significantly increased, by more than factors of 2 and 3 in each deforming case, respectively. Part of this increase is due to the combination of the intense deformation pushing water backward on the onshore side of the slide and the fact that the present case corresponds to a fairly shallow initial depth of submergence, which intensifies the former effect. Another contribution to the increase in runup is the larger elevation wave created after the initial drawdown for deforming slides.

In considering these results, one should keep in mind that slide deformation was modeled very crudely and extreme extension rates were used in these simulations. Moreover, mitigating factors such as slide thickness and density reduction during motion were neglected. Nevertheless, intense slide deformation in shallow water would appear to significantly increase coastal hazard and should thus be investigated more carefully and realistically.

### Effects of Mass Failure Type

Eq. (12), derived for the center of mass motion of a slide, differs from that, Eq. (19), of a slump. Both equations, however, have the same small time approximation  $S \approx a_o t^2 / 2$ . Hence, given the same shape, dimensions ( $B, T$ ) (and thus  $C_m$ ), submergence depth  $d$ , and density  $\gamma$ , slide and slump motions should be identical for small times, provided they have the same initial acceleration  $a_o$ . Based on the preceding equations, this occurs if, for the slump,  $\Delta\Phi = 2 \sin \theta$  (assuming  $\psi = 0$  for the slide). With identical  $a_o$ , tsunami features of similar slides and slumps should also initially be similar. In addition, if one specified that characteristic times  $t_o$  are also identical, the slide terminal velocity  $u_t$  would also match the slump maximum velocity  $u_{max}$ , making tsunami features similar over an even longer time (of order  $t_o$ ). Based on the preceding equations, this occurs if, for the slump,  $R' = \pi(\gamma + C_m) / (2C_d \sin \theta)$  (assuming  $\psi = 0$  for the slide).

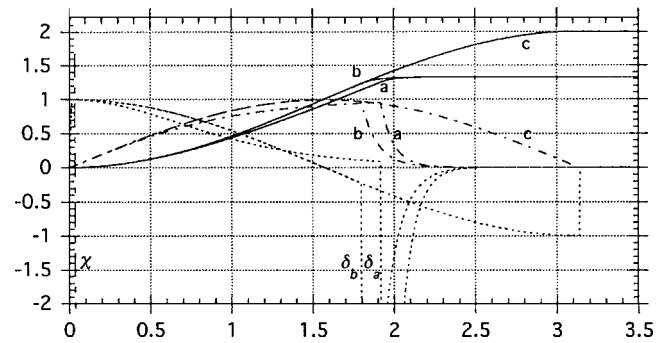


Fig. 9. SMF kinematics specified in 2D model [Eqs. (12)–(21) and (24)–(30); Fig. 1], for slide (a) and slumps (b:  $R' = 17.3$ , c:  $R' = 1$ ) of Fig. 10;  $S/S_o$  (—),  $\dot{S}/u_t$  (---),  $\ddot{S}/a_o$  (.....)

The latter requirement combined with the former yields  $2S'_o = \pi(\gamma + C_m) / C_d \approx 8.95$  for typical reference values. We will show in Part II that, while the similarity in initial accelerations may yield realistic values for the angular displacement  $\Delta\Phi$  of actual slumps, the similarity of characteristic times greatly overestimates maximum slump displacement. Indeed, a typical slump only travels up to about 50% of its length, i.e.,  $2S'_o \leq 0.5$ .

We illustrate these considerations by calculating kinematics and corresponding tsunami features for a slump moving down a slope with  $\theta = 15^\circ$  in a domain with maximum depth  $h'_o = 2$ . The slump has reference thickness  $T'_{ref} = 0.052$ , density  $\gamma_{ref} = 1.85$ , and initial depth  $d'_{ref} = 0.259$ , and its shape is described by Eqs. (1) and (2), with  $\varepsilon = 0.75$  and  $C_m = 1$ . Slump kinematics and generated tsunami features are compared to those of a slide of identical characteristics, and  $C_d = 1$ . We simulate two slumps satisfying the first requirement earlier, i.e., with  $\Delta\Phi = 0.518$ , leading to  $a'_o = 0.0772$  for both slide and slumps. We will see in Part II that this angular displacement is quite typical for slumps. With Eq. (20), we find  $C_n = 0.268$  for both slumps and, hence, with Eq. (17), the same shear stress,  $S_u = 0.249(\rho_\ell - \rho_w)gT$ . For the first slump, we also specify the second requirement, yielding  $R' = 17.3, t'_o = 7.616$ , as for the slide, and  $u'_{max} = u'_t = 0.588$ . For the second slump, we take a typical value  $2S'_o = 0.518$  or  $R' = 1$ , which yields  $t'_o = 1.831$  and  $u'_{max} = 0.141$ .

Fig. 9 shows the center of mass motion, velocity, and acceleration specified for the slide (a) and the two slumps, (b) and (c). Both slide (a) and slump (b) exhibit very similar kinematics and do not reach their larger maximum displacement, but decelerate at time  $t = \delta t_o$  to come to rest at the toe of the slope. Slump (c), by contrast, completes its full theoretical displacement. Fig. 10 shows simulated tsunami features. As expected, slump (b) and slide (a) have very similar tsunami elevations at gauge  $x'_g$  and runup, up to  $t \sim 1.5t_o$ . Larger differences can be seen at the far field gauges at  $x' = 4$  and  $7$ . For slump (c), despite the same initial acceleration, tsunami elevations are much smaller at all gauges, particularly in the far field, with the exception of the first trough to crest difference calculated at gauge  $x'_g$ , which is more directly related to the initial acceleration and is thus similar to that of the other two cases. Correlatively, the first rundown depression wave caused by slump (c) is quite close to that produced by slide (a) or slump (b), although the first positive runup is much smaller. Due to its smaller characteristic time, slump (c) also initially produces shorter waves.

Thus, assuming a realistic maximum displacement for a

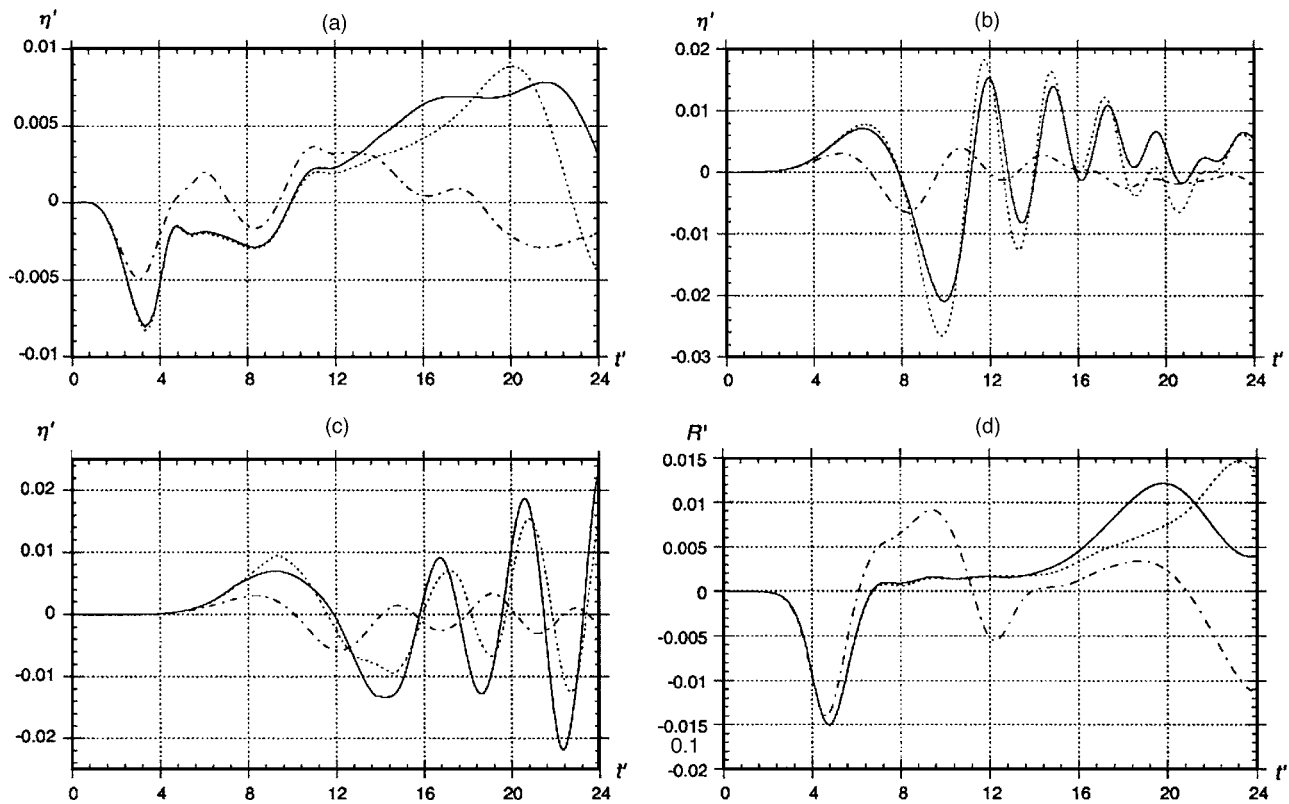


**Fig. 10.** Tsunami sensitivity to SMF type, for slide with parameters as in Fig. 7 (—) and slumps with  $C_d=0$ ,  $C_n=0.286$ ,  $\Delta\Phi=0.518$ , and  $R'=17.3$  (----); 1 (---): (a) gauge elevation at  $x'_g=1.168$ ; (b) gauge elevation at  $x'=4$ ; (c) gauge elevation at  $x'=7$ ; and (d) coastal runoff

slump, everything else being equal, we see that a slump generates a much smaller tsunami than the equivalent slide, particularly in the far field.

### Tsunami Amplitude and Runup for Rigid Slides

The effect of initial submergence depth on tsunami amplitude and runup is studied for a rigid slide in Figs. 11–13. Parameters of the slide are identical to those of the rigid slide shown in Figs. 7 and 8, for which only  $d'_{ref}=0.259$  was modeled. Here, nine depths varying in the range  $d'=0.125$  to  $0.625$  are successively studied. Fig. 11(a) shows spatial free surface elevations calculated at the time when maximum drawdown occurs at  $x=x_g$  (where the characteristic amplitude  $\eta_o$  is measured); in each case, a wave of depression surrounds  $x=x_g$  and a “bounce back,” offshore moving wave of elevation occurs for larger  $x$ . In Figs. 11(b and c), for later times corresponding to  $t_o$  and  $2t_o$ , these initial waves transform into oscillatory wave trains, indicative of dispersive effects (only five cases are shown to simplify the figures). Fig. 12(b), which shows  $\eta'(t)$  calculated at  $x'=4$ , further illustrates these dispersive features. In Fig. 11(a) for the shallowest slides, f to i, a large rundown simultaneously occurs at the shore while runup occurs for the deeper slide cases, a to e. Fig. 12 shows temporal variations, which are helpful in better interpreting these results. In Fig. 12(a), which shows surface elevations at  $x_g$ , we see: (1) initial depression waves, responsible for  $\eta_o$ , are followed by positive bounce-back waves; this happens rather soon for the shallowest cases but much later for the deeper cases; (2) the bounce-back waves [also clearly visible in Fig. 11(b) for small  $x$ ] propagate shoreward and are responsible for maximum runup; (3) in the shallower cases, further oscillations follow the bounce-back waves, due to reflection coming back from shore, following maxi-

imum runup; and (4) the temporal runup variation is shown in Fig. 12(c). In the shallower cases, rundown is larger than runup in absolute terms, while this trend reverses itself for the deeper cases. This is likely because the bounce-back waves, which cause runup, only have a short distance of propagation in the shallower cases before interacting with the shore and, hence, not enough time to steepen up. For the deeper cases, the bounce-back waves have both enough distance and time to significantly shoal up before maximum runup occurs.

Fig. 13 summarizes results of Figs. 11 and 12 in terms of characteristic amplitude and maximum runup/rundown, as a function of initial submergence depth. In Fig. 13(a), curve fitting yields  $\eta_o/\eta_{ref} \propto (d/d_{ref})^{-1.25}$ . In Figs. 13(b and c), maximum runup  $R_u$  and rundown  $R_d$  are shown for domain depth  $h'_o=2$  [from Fig. 12(c)] and 1 (as initially used), respectively. While rundown is not strongly affected by a change in domain depth, runup increases in the shallower domain because, as discussed before, the specified slide deceleration occurs in shallower water, in order for the slide to come to a stop at the toe of the slope. This somewhat enhances the (runup causing) bounce-back wave, particularly for the smaller initial submergence depths. Two depth regions can also be seen in each of the figures for both  $R_u$  and  $R_d$ . The shallower regions, in which  $d_{ref}/d > 1$ , correspond to shorter, steeper, and thus more nonlinear tsunami waves, for which the bounce-back waves more strongly interact with the shoreline. Note, in Fig. 13(b), around the reference depth, maximum runup occurs for the second arriving wave.

As for the characteristic amplitudes, runup and rundown results follow simple power curve fits of submergence depth, indicating that runup is simply related to tsunami characteristic amplitudes by similarly simple power laws. In fact, for  $d/d_{ref} > 1$  in

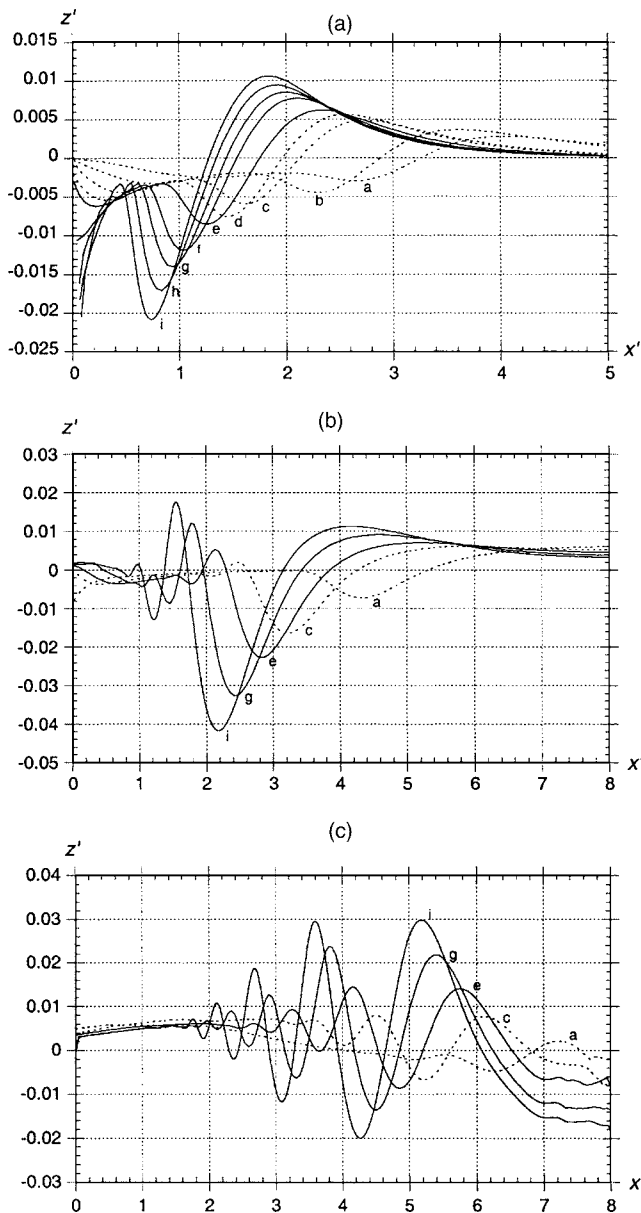


**Fig. 11.** Tsunami amplitude for rigid slides, with  $\theta=15^\circ$ ,  $\gamma=1.85$ ,  $C_m=1$ ,  $C_d=1$ ,  $C_n=0$ ,  $h'_o=2$ ,  $T'=0.052$ ,  $\chi=0.02$ ,  $f=0.10$ , and  $\varepsilon=0.75$ . Spatial variation as function of submergence depth,  $d'=a:0.625$ ; b: 0.500; c: 0.350; d: 0.300; e: 0.259 ( $d'_{ref}$ ); f: 0.200; g: 0.175; h: 0.150; i: 0.125;  $t$  equals: (a)  $t(\eta_o)$ ; (b)  $t_o$ ; (c)  $2t_o$ .

Fig. 13(b),  $R_u/d \propto (\eta_o/\eta_{ref})^{1.09}$ , and there is an almost *one on one correspondence* between relative runup and tsunami characteristic amplitude. In Fig. 13(b), we find the total runup,  $(R_u+R_d)/d \propto (d/d_{ref})^{-1.21}$ , and the exponent is  $-1.40$  in Fig. 13(c). This measures the total water vertical elevation on the shore, between run-down and runup.

### Two-Dimensional Criteria

The 2D simulations presented here only apply to SMFs for which  $w \gg b$ . Other work by the writers, reported in separate papers, deals with the 3D modeling of SMF tsunamis, for which sensitivity analyses of tsunami features to SMF width were performed (Grilli and Watts 2001; Grilli et al. 2002; Vogelmann 2001). Based on this 3D work, we propose two additional criteria for

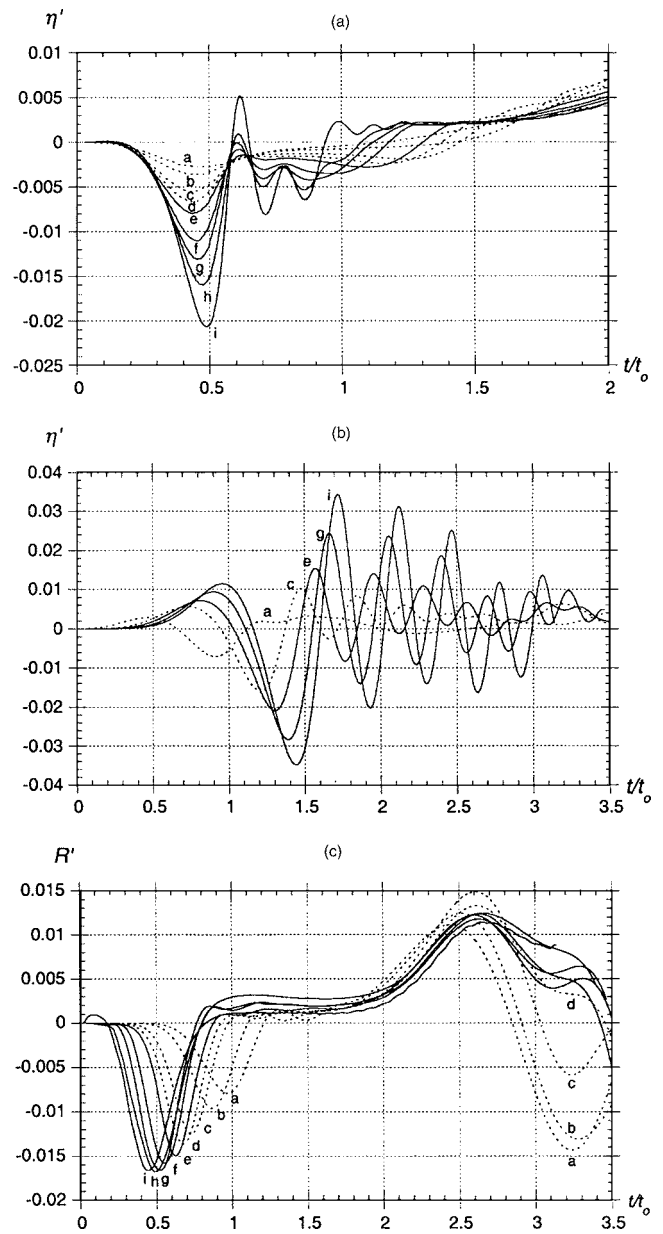


**Fig. 12.** Tsunami amplitude and runup for rigid slides, as function of submergence depth; same simulation cases as in Fig. 11. Time variation for: (a)  $\eta'(x'_g)$ ; (b)  $\eta'(x'=4)$ ; and (c)  $R'$ .

assessing the applicability of 2D tsunami generation to actual 3D tsunamis and, correlatively, of predictive equations of 2D tsunami amplitude presented in Part II:

$$w \gg d, \quad w \gg \lambda_o \quad (23)$$

Hence, the SMF width must be much greater than the local water depth as well as the characteristic tsunami wavelength, in order to generate tsunamis that are only mildly affected by the third spatial dimension (i.e., quasi-2D) during initial times. When Eq. (23) is not met, 3D tsunami generation should be computed. Depth and wavelength are length scales that represent SMF geometry and dynamics, respectively. Eq. (23) shows that characteristic wavelength is also a measure of lateral tsunami propagation during generation, which affects tsunami amplitude. This effect is quantified in Part II.

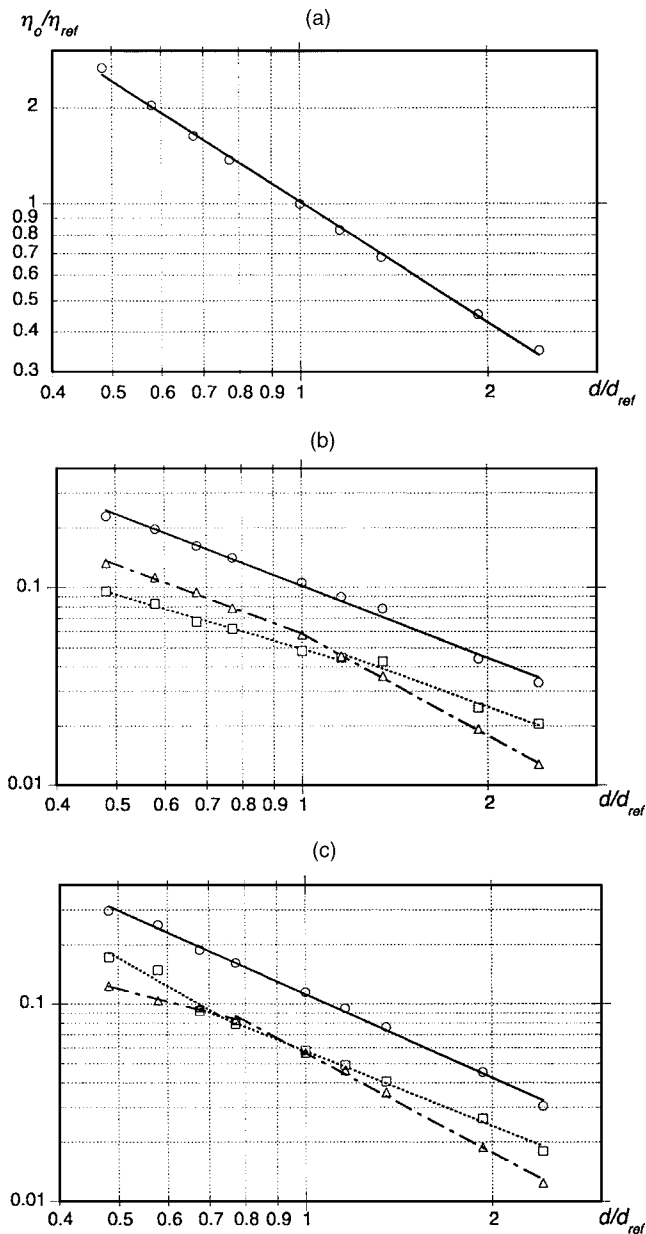


**Fig. 13.** Tsunami characteristics as function of submergence depth, for cases of Figs. 4, 11, and 12: (a) characteristic amplitude ( $\circ$ ) for  $h'_o=2$  [Fig. 12(a)]; (b) runup for  $h'_o=2$  [Fig. 12(c)]; (c) runup for  $h'_o=1$  [symbols in (b) and (c) indicate ( $\square$ )  $R_u/d$ ; ( $\Delta$ )  $R_d/d$ ; ( $\circ$ )  $(R_u+R_d)/d$ ]

## Conclusions

Two-dimensional numerical simulations were presented, using a modified version of the 2D-FNPF model of Grilli and Watts (1999), for tsunami generation by two types of SMFs: underwater slides and slumps.

The model was experimentally validated for tsunami generation by slides; model results reproduced laboratory results quite well and certainly within the accuracy of experimental measurements. Hence, the model was used to study tsunami features as a function of parameters describing SMF geometry, type, and kinematics. The main advantage of conducting numerical rather than laboratory experiments is that the model can more easily and efficiently cover a much broader range of physical parameters

than can be readily performed in a laboratory. Numerical results are available everywhere in the computational domain and not just at gauge or probe locations. Considering the small laboratory scales used for tsunamis, both scale effects and local perturbations due to instruments also become factors affecting experimental accuracy.

We showed that, for rigid slides of Gaussian shape, both near and far field tsunami amplitudes increase if shape spreading decreases. Hence, to the limit, the largest tsunamis are generated when assuming a semielliptical shape, as in Grilli and Watts' (1999) original work. Accordingly, in Part II, to produce worst case scenarios, curve fits of characteristic tsunami amplitudes are based on computations with semielliptical SMFs.

We showed that, for slides, a reasonable rate of deformation during motion has little effect on near field tsunami features, but more significantly affects far field features. An extreme rate of deformation, however, significantly affects both near and far field tsunami features. In particular, coastal runup may be significantly increased, hence increasing coastal hazard. Due to the crude representation of slide deformation in these studies, however, more detailed and realistic simulations of deforming slides should be performed in future work before more definite conclusions are drawn. Specifically, effects of changes in slide thickness, length, and possibly density, and gradual development of a forward bulge in the slide shape, as shown in Watts and Grilli's (2003) computations, should be simulated.

We compared tsunami features computed for underwater slides and slumps of identical density and geometry. Assuming the slump parameters are set within the typical range, we found that smaller tsunami amplitudes and wavelengths were generated than for a slide, particularly in the far field. This can be explained by the fact that: (1) the duration of acceleration is proportional to  $t_o$ , and therefore lasts longer for a slide; and (2) the tsunami amplitude scales foremost with SMF displacement, which is smaller for slumps.

Finally, the effect of initial submergence depth is studied for a rigid slide, and a detailed analysis of tsunami amplitude and runup is made. The characteristic tsunami amplitude  $\eta_o$  is found to grow inversely proportional to the power 1.25 of initial submergence depth  $d$ . This exponent is similar to that given by Green's law, for the relative height of linear long waves, shoaling over slopes. Runup and rundown at the coastline also grow inversely proportional to a small power of depth, and hence proportional to a power of characteristic tsunami amplitude. Exponents are different when  $d/d_{ref}$  is smaller or larger than one, i.e., for strongly or weakly nonlinear tsunamis.

Further parametric analyses in Part II will show that the dependence of  $\eta_o$  on  $d$  is general for tsunamis generated by rigid slides, independent of slope angle or slide thickness. These analyses will also show that slide volume (and hence dimensionless thickness) is the second important physical parameter governing tsunami generation, and its effect will be quantified. While Part I of this work has been largely theoretical, we will demonstrate in Part II that our results may offer a useful description of tsunami generation by actual SMFs. In particular, we will derive predictive equations for 2D SMF tsunami characteristic amplitudes and propose an approximate analytic representation for 3D tsunami surface elevation that can be used to perform case studies.

It should finally be pointed out that Part I only reports on the initial stages of research, which has been ongoing for the past six years, when only 2D FNPF simulations of SMF tsunamis were available. Later developments included the implementation of a 3D FNPF model for SMF tsunami (Grilli and Watts 2001; Grilli

et al. 2002) and the subsequent refinement of the predictive equations (this is discussed to some extent in Part II).

## Appendix. Motion Ramp-Up and Deceleration for Slides or Slumps

In the slide/slump motion ramp-up period, for  $t \in [0, t_i]$ , the kinematics specified in the numerical model are given by (e.g., Fig. 3 for slides):

$$a = \frac{a_i}{2} \left( 1 + \frac{\tanh(k_r t - \tau_r)}{\tanh \tau_r} \right)$$

$$u' = \frac{a_i}{2} \left( \frac{\ln(\cosh(k_r t - \tau_r)) - \ln(\cosh \tau_r)}{k_r \tanh \tau_r} \right)$$

$$u = \frac{a_i}{2} t + u'$$

$$S = \frac{a_i}{4} t^2 + \int_0^t u'(t') dt' \quad (24)$$

where  $\tau_r = 3$ ;  $k_r = 2\tau_r/t_i$ ; and  $a_i = \ddot{S}(t_i)$  from Eqs. (16) or (21), for slides or slumps, respectively.

To determine the slide deceleration region, we first calculate the maximum allowable center of mass motion  $S^{max}$

$$S^{max} = \frac{1}{\cos \theta} (x_o - x_i) - \frac{b}{2} \quad (25)$$

and time to reach it,  $t^{max}$ , found for slides from Eq. (12) as

$$t^{max} = t_o \operatorname{acosh} \left( \exp \left\{ \frac{S^{max} - S_i}{S_o} \right\} \cosh \frac{t_i}{t_o} \right) \quad (26)$$

and for slumps from Eq. (19) as

$$t^{max} = t_o \operatorname{acos} \left( \cos \frac{t_i}{t_o} - \frac{S^{max} - S_i}{S_o} \right) \quad (27)$$

where  $S_i$  denotes  $S(t_i)$ . Hence, in the slide/slump deceleration region, for  $t > \delta t_o$ , the SMF kinematics are given by

$$S = S_\Delta + \Delta_S (1 - \exp\{-k_S(t - \delta t_o)\})$$

$$\dot{S} = k_S \Delta_S \exp\{-k_S(t - \delta t_o)\}$$

$$\ddot{S} = -k_S^2 \Delta_S \exp\{-k_S(t - \delta t_o)\} \quad (28)$$

with  $\delta = t^{max}/t_o - f$  ( $f$  is typically 10%);  $\Delta_S = S^{max} - S_\Delta$ ;  $k_S = u_\Delta/\Delta_S$ ; and

$$S_\Delta = S_i + S_o \ln \left( \frac{\cosh \delta}{\cosh \frac{t_i}{t_o}} \right)$$

$$u_\Delta = u_i + u_t \left( \tanh \delta - \tanh \frac{t_i}{t_o} \right) \quad (29)$$

for slides and

$$S_\Delta = S_i + S_o \left( \cos \frac{t_i}{t_o} - \cos \delta \right)$$

$$u_\Delta = u_i + u_{max} \left( \sin \delta - \sin \frac{t_i}{t_o} \right) \quad (30)$$

for slumps. In between these regions, for  $t \in [t_i, \delta t_o]$ , Eqs. (12)–(16) or (19)–(21) are used to describe the SMF kinematics.

For deforming slides, the expanding length Eq. (22) for  $B$  is modified in the deceleration region, for  $t > \delta t_o$ , as

$$B = B_\Delta + \Delta_B (1 - \exp\{-k_S(t - \delta t_o)\})$$

$$\dot{B} = k_S \Delta_B \exp\{-k_S(t - \delta t_o)\}$$

$$\ddot{B} = -k_S^2 \Delta_B \exp\{-k_S(t - \delta t_o)\} \quad (31)$$

with  $B_\Delta = B(\delta t_o)$  from Eq. (22) and  $\Delta_B = B(t^{max}) - B_\Delta$ .

## Acknowledgments

The research reported here was partly supported by Grant CMS-0100223 from the National Science Foundation, and by Applied Fluids Engineering, Inc. Partial support for the second writer was also provided by the Federal Emergency Management Agency, under Grant DR-1008-9004 made to Costas Synolakis at the University of Southern California. The writers benefited from discussions with Drs. Fumi Imamura and Costas Synolakis. Aaron Bengston is acknowledged for his help in performing the laboratory experiments.

## References

- Assier-Rzadkiewicz, S., Mariotti, C., and Heinrich, P. (1997). "Numerical simulation of submarine landslides and their hydraulic effects." *J. Waterw., Port, Coastal, Ocean Eng.*, 123(4), 149–157.
- Bardet, J.-P. (1997). *Experimental soil mechanics*, Prentice-Hall, Upper Saddle River, N.J.
- Dobry, R., Ladd, R. S., Yokel, F. Y., Chung, R. M., and Powell, D. (1982). "Prediction of pore water pressure buildup and liquefaction of sands during earthquakes by the cyclic strain method." *NBS Building Science Series 138*, National Bureau of Standards, Washington, D.C.
- Edgers, L., and Karlsrud, K. (1982). "Soil flows generated by submarine slides: Case studies and consequences." *Nor. Geotech. Inst. Bull.*, 143, 1–11.
- Enet, F., Grilli, S. T., and Watts, P. (2003). "Laboratory experiments for tsunamis generated by underwater landslides: Comparison with numerical modeling." *Proc., 13th Offshore and Polar Engineering Conf.*, International Society of Offshore and Polar Engineers, Cupertino, Calif., 3, 372–379.
- Fine, I. V., Rabinovich, A. B., Kulikov, E. A., Thomson, R. E., and Bornhold, B. D. (1998). "Numerical modelling of landslide-Generated tsunamis with application to the Skagway Harbor tsunami of November 3, 1994." *Proc. Tsunami Symp.*, Paris.
- Fontaine, E. (2000). "On the use of smoothed particle hydrodynamics to model extreme waves and their interaction with structures." *Proc., Rogue Waves 2000*, Ifremer, Brest, France.
- Gomez-Gesteira, M., and Dalrymple, R. A. (2004). "Using a three-dimensional smoothed particle hydrodynamics method for wave impact on a tall structure." *J. Waterw., Port, Coastal, Ocean Eng.*, 130(2), 63–69.
- Grilli, S. T. (1997). "Fully nonlinear potential flow models used for long wave runup prediction." *Long-wave Runup Models*, H. Yeh, P. Liu, and C. Synolakis, eds. World Scientific, Singapore, 116–180.
- Grilli, S. T., and Horrillo, J. (1997). "Numerical generation and absorption of fully nonlinear periodic waves." *J. Eng. Mech.*, 123(10), 1060–1069.

- Grilli, S. T., Skourup, J., and Svendsen, I. A. (1989). "An efficient boundary element method for nonlinear water waves." *Eng. Anal. Boundary Elem.*, 6(2), 97–107.
- Grilli, S. T., and Subramanya, R. (1996). "Numerical modeling of wave breaking induced by fixed or moving boundaries." *Comput. Mech.*, 17(6), 374–391.
- Grilli, S. T., Subramanya, R., Svendsen, I. A. and Veeramony, J. (1994). "Shoaling of solitary waves on plane beaches." *J. Waterw., Port, Coastal, Ocean Eng.*, 120(6), 609–628.
- Grilli, S. T., Svendsen, I. A., and Subramanya, R. (1997). "Breaking criterion and characteristics for solitary waves on slopes." *J. Waterw., Port, Coastal, Ocean Eng.*, 123(3), 102–112.
- Grilli, S. T., Svendsen, I. A., and Subramanya, R. (1998). "Closure to 'Breaking criterion and characteristics for solitary waves on slopes'." *J. Waterw., Port, Coastal, Ocean Eng.*, 124(6), 333–335.
- Grilli, S. T., Vogelmann, S., and Watts, P. (2002). "Development of a 3D numerical wave tank for modeling tsunami generation by underwater landslides." *Eng. Anal. Boundary Elem.*, 26(4), 301–313.
- Grilli, S. T., and Watts, P. (1999). "Modeling of waves generated by a moving submerged body: Applications to underwater landslides." *Eng. Anal. Boundary Elem.*, 23(8), 645–656.
- Grilli, S. T., and Watts, P. (2001). "Modeling of tsunami generation by an underwater landslide in a 3D numerical wave tank." *Proc., 11th Offshore and Polar Engineering Conf.*, International Society for Offshore and Polar Engineers, Cupertino, Calif., 3, 132–139.
- Hampton, M. A., Lee, H. J., and Locat, J. (1996). "Submarine landslides." *Rev. Geophys.*, 34(1), 33–59.
- Harbitz, C. B. (1992). "Model simulations of tsunamis generated by the Storegga slides." *Mar. Geol.*, 105, 1–21.
- Heinrich, P. (1992). "Nonlinear water waves generated by submarine and aerial landslides." *J. Waterw., Port, Coastal, Ocean Eng.*, 118(3), 249–266.
- Imamura, F., and Gica, E. C. (1996). "Numerical model for tsunami generation due to subaqueous landslide along a coast." *Sci. Tsunami Hazards*, 14, 13–28.
- Iwasaki, S. (1982). "Experimental study of a tsunami generated by a horizontal motion of a sloping bottom." *Bull. Earthquake Res. Inst., Univ. Tokyo* 57, 239–262.
- Iwasaki, S. (1987). "On the estimation of a tsunami generated by a submarine landslide." *Proc., Int. Tsunami Symp.*, Vancouver, Canada, 134–138.
- Iwasaki, S. (1997). "The wave forms and directivity of a tsunami generated by an earthquake and a landslide." *Sci. Tsunami Hazards*, 15, 23–40.
- Jiang, L., and LeBlond, P. H. (1992). "The coupling of a submarine slide and the surface waves which it generates." *J. Geophys. Res.*, 97(8), 12,731–12,744.
- Jiang, L., and LeBlond, P. H. (1993). "Numerical modeling of an underwater Bingham Plastic mudslide and the waves which it generates." *J. Geophys. Res.*, 98(6), 10,303–10,317.
- Jiang, L., and LeBlond, P. H. (1994). "Three-dimensional modeling of tsunami generation due to a submarine mudslide." *J. Phys. Oceanogr.*, 24, 559–573.
- Keating, B. H., and McGuire, W. J. (2000). "Island edifice failures and associated tsunami hazards." *Pure Appl. Geophys.*, 157, 899–955.
- Lee, H. J., Schwab, W. C., Edwards, B. D., and Kayen, R. E. (1991). "Quantitative controls on submarine slope failure morphology." *Mar. Geotech.*, 10, 143–157.
- Lynett, P., and Liu, P. L.-F. (2003). "A numerical study of submarine-landslide-generated waves and runup." *Proc. Roy. Soc. Lond., Coast, and Oc. Engrg. A*, 458, 2,885–2,910.
- Murty, T. S. (1979). "Submarine slide-generated water waves in Kitimat Inlet, British Columbia." *J. Geophys. Res.*, 84(12), 7,777–7,779.
- Nayfeh, A. H., and Mook, D. T. (1979). *Nonlinear oscillations*, Wiley, New York.
- Prior, D. B., and Coleman, J. M. (1979). "Submarine landslides: Geometry and nomenclature." *Z. Geomorph. N. F.*, 23(4), 415–426.
- Schwab, W. C., Lee, H. J., and Twichell, D. C. (1993). "Submarine landslides: Selected studies in the U.S. exclusive economic zone." *Bulletin 2002, U.S. Geological Survey*, Reston, Va.
- Seed, H. B., Seed, R. B., Schlosser, F., Blondeau, F., and Juran, I. (1988). "The landslide at the Port of Nice on October 16, 1979." *Rep. No. UCB/EERC-88/10*, Earthquake Engineering Research Center, Berkeley, Calif.
- Striem, H. L., and Miloh, T. (1976). "Tsunamis induced by submarine slumping off the coast of Israel." *Int. Hydrographic Rev.*, 2, 41–55.
- Synolakis, C. E., et al. (2002). "The slump origin of the 1998 Papua New Guinea tsunami." *Proc. R. Soc. London, Ser. A*, 458, 763–790.
- Tappin, D. R., Watts, P., McMurtry, G. M., Lafoy, Y., and Matsumoto, T. (2001). "The Sissano, Papua New Guinea tsunami of July 1998—Offshore evidence on the source mechanism." *Mar. Geol.*, 175, 1–23.
- Tappin, D. R., Watts, P., McMurtry, G. M., Lafoy, Y., and Matsumoto, T. (2002). "Prediction of slump generated tsunamis: The July 17th 1998 Papua New Guinea event." *Sci. Tsunami Hazards*, 20(4), 222–238.
- Thomson, R. E., Rabinovich, A. B., Kulikov, E. A., Fine, I. V., and Bornhold, B. D. (2001). "Numerical simulation of the landslide-generated tsunami of November 3, 1994 in Skagway Harbor, Alaska." *Tsunami Research at the End of a Critical Decade*, G. T. Hebenstreit, ed., Klüwer Academic, Boston, 243–282.
- Tinti, S., and Bortolucci, E. (2000). "Analytical investigation on tsunamis generated by submarine slides." *Annali de Geofisica*, 43, 519–536.
- Tinti, S., Bortolucci, E., and Chiavettieri, C. (2001). "Tsunami excitation by submarine slides in shallow-water approximation." *Pure Appl. Geophys.*, 158, 759–797.
- Titov, V. V., and Gonzalez, F. I. (2001). "Numerical study of the source of the July 17, 1998 PNG tsunami." *Tsunami Research at the End of a Critical Decade*, G. T. Hebenstreit, ed., Kluwer, Dordrecht, The Netherlands, 197–207.
- Todorovska, M. I., Hayir, A., and Trifunac, M. D. (2002). "A note on tsunami amplitudes above submarine slides and slumps." *Soil Dyn. Earthquake Eng.*, 22, 129–141.
- Turner, A. K., and Schuster, R. L. (1996). "Landslides: Investigation and mitigation." *Special Rep. 247*, Transportation Research Board, Washington, D.C.
- Verriere, M., and Lenoir, M. (1992). "Computation of waves generated by submarine landslides." *Int. J. Numer. Methods Fluids*, 14, 403–421.
- Vogelmann, S. (2001). "Sensitivity study of numerical simulation of tsunamis generated by submarine slope failure." MS thesis, Univ. of Rhode Island, Kingston, R.I.
- Ward, S. N. (2001). "Landslide tsunami." *J. Geophys. Res.*, 106(6), 11201–11215.
- Watts, P. (1997). "Water waves generated by underwater landslides." PhD thesis, California Institute of Technology, Pasadena, Calif.
- Watts, P. (1998). "Wavemaker curves for tsunamis generated by underwater landslides." *J. Waterw., Port, Coastal, Ocean Eng.*, 124(3), 127–137.
- Watts, P. (2000). "Tsunami features of solid block underwater landslides." *J. Waterw., Port, Coastal, Ocean Eng.*, 126(3), 144–152.
- Watts, P., and Grilli, S. T. (2003). "Underwater landslide shape, motion, deformation, and tsunami generation." *Proc., 13th Offshore and Polar Engineering Conf.*, International Society of Offshore and Polar Engineers, Cupertino, Calif., 3, 364–371.
- Watts, P., Grilli, S. T., Kirby, J. T., Fryer, G. J., and Tappin, D. R. (2003). "Landslide tsunami case studies using a Boussinesq Model and a fully nonlinear tsunami generation model." *Nat. Hazards Earth Syst. Sci.*, 3, 391–402.
- Watts, P., Imamura, F., and Grilli, S. T. (2000). "Comparing model simulations of three benchmark tsunami generation cases." *Sci. Tsunami Hazards*, 18(2), 107–124.
- Wei, J., Kirby, J. T., Grilli, S. T., and Subramanya, R. (1995). "A fully nonlinear Boussinesq Model for surface waves. Part 1. Highly nonlinear unsteady waves." *J. Fluid Mech.*, 294, 71–92.
- Wiegel, R. L. (1955). "Laboratory studies of gravity waves generated by the movement of a submarine body." *Trans., Am. Geophys. Union*, 36(5), 759–774.